

Final Technical Report for USGS Awards G14AP00044 & G14AP00045

**Rupture Direction, Hanging Wall, Basin, and Distance Effects on Ground Motions from
Large Normal-Faulting Earthquakes: Collaborative Research with San Diego State
University and the University of Utah**

by

Nan Wang, Daniel Roten, Kim B. Olsen, and James C. Pechmann

**Period of Award (with no-cost extension):
September 1, 2014, to August 30, 2016**

Principal Investigators:

Kim B. Olsen
San Diego State University, GMCS 231A
San Diego, CA 92182
Ph: 619-594-2649
Email: kbolsen@mail.sdsu.edu

James C. Pechmann
University of Utah
Department of Geology and Geophysics
115 South 1460 East Room 383 FASB
Salt Lake City, UT 84112-0102
Ph 801-581-3858
Email: pechmann@seis.utah.edu

Research supported by the U.S. Geological Survey (USGS), Department of the Interior, under USGS award numbers G14AP00044 and G14AP00045. The views and conclusions contained in this document are those of the authors and should not be interpreted as necessarily representing the official policies, either expressed or implied, of the U.S. Government.

Summary

We have analyzed numerical simulations of six M7 earthquakes on the Salt Lake City segment of the Wasatch Fault (WF), Utah, to better understand the long-period ground motions that these simulations predict in the adjacent Salt Lake Valley (SLV). We calculated peak spectral accelerations at 2s (SA-2s) and 3s (SA-3s) in an updated Wasatch Front Community Velocity Model (WFCVM-v3d) as well as in a 1D rock model, using the same fault rupture descriptions as in Roten et al. (2011), in order to separate source and basin effects. The SAs from the 1D model are generally smoother and smaller in amplitude due to higher V_{s30} values and the lack of underlying 3D structure. 3D/1D ratios of the SA values depict the 3D basin effects in the SLV, such as focusing, defocusing, and entrapment of waves in the basin, particularly above the deeper parts of the basin. The SA-2s and SA-3s values show a strong correlation [0.6 to 0.8] with two basin depth measurements in the WFCVM, with a smaller (negative) correlation to V_{s30} [-0.3 to -0.6]. Based on this result, we developed regression models for the 6-scenario ensemble of ground motions as a function of depth to the isosurfaces of $V_s=1.0$ km/s and 1.5 km/s in the SLV. The models for the 1.0 km/s isosurface show amplification factors of up to ~ 2.7 and ~ 3.7 above the deepest part of the basin for SA-2s and SA-3s, respectively.

We find correlations between the long-period scenario ground motions in the SLV and the underlying fault slip that range from 0.55 to 0.87. The correlations with peak slip rate are somewhat lower, ranging from 0.41 to 0.80. The correlations are larger for the simulations using the 3D basin model, as compared to those obtained from the 1D model, suggesting an interaction between the source characteristics and the basin structure. To assess how well a simple parametric directivity model can explain the long-period ground motion patterns for the individual M7 WF scenarios, we compute directivity factors using the Bayless and Somerville (2013) model. The directivity effects from this parametric model increase the SA-2s and SA-3s values by less than 30% for the scenarios, and increase the similarity between the NGA-West2 GMPEs and simulations in less than half of the cases examined.

As compared to predictions from four NGA-West2 GMPEs, the long-period WF scenario ground motions on soil sites show a gradual increase in bias from $R_{rup}=0$ to 1-1.5 km and a decrease in bias from $R_{rup} \sim 4$ km to ~ 10 km, with both trends about twice as large in the 3D as in the 1D simulations. The resulting high in the bias plots for $R_{rup} \sim 1-4$ km appears to be partly caused by the basin edge effect and/or entrapment of waves in the deeper parts of the basin, combined with scenario specific conditions such as slip distributions not captured by the GMPEs. However, the presence of the near-fault bias in the 1D simulations (albeit smaller than in the 3D results) suggests that the use of velocity strengthening in the near-surface part of the rupture models also contributes to decreasing the SAs within ~ 1.5 km of the fault. Tests with a less attenuating Q model than used by Roten et al. (2011) indicates that uncertainties in the Q distribution is likely not contributing to the near fault bias.

Three NGA-West2 GMPEs with explicit hanging wall factors do a reasonably good job of predicting the increased ground motions over the hanging wall for SA-3s. For SA-2s, the simulations show minimal increase over the hanging wall and the GMPEs overpredict the simulations, but the overpredictions are less than one standard deviation.

Final Technical Report

Introduction

Roten et al. (2011) simulated 0-1 Hz 3-D numerical simulations of ground motions from M 7 earthquakes on the Salt Lake City segment of the Wasatch fault in Utah (WFSLC) for six different rupture scenarios. The simulations were carried out in the Wasatch Front Community Velocity Model (WFCVM), which includes the low-velocity sediments of the Salt Lake Basin adjacent to the WFSLC. These sediments have a strong influence on the ground shaking. For example, the 3D simulations show much larger 0-1 Hz Spectral Accelerations (SAs) on the sediments in the Salt Lake Valley, as compared to bedrock and thin sediment sites on the footwall, with highly variable patterns dependent on the specific scenario. Average ground motions from the six scenarios were generally consistent with values predicted by four next-generation attenuation (NGA-West1) models, but with some differences.

In this study, we build on the results by Roten et al. (2011) to separate and quantify the effects of four important factors on strong ground motions from large normal-faulting earthquakes on the WFSLC: rupture direction, location on the hanging wall versus the footwall, the deep 3-D structure of the Salt Lake Basin, and the distance from the rupture in the near field range. To investigate these effects, we simulate the six scenarios from Roten et al. (2011) with an updated version of the WFCVM, as well as with a 1-D rock site velocity model. We use the two sets of simulations to analyze the relationships between SA-2s and SA-3s and basin depth, V_{s30} , source description, and directivity models. Finally, we compare the results to the more recent NGA-West2 models and discuss the differences.

Ground Motion Amplification Due to Basin Structure

Effects of Basin Depth and V_{s30}

We recalculated the six M7 Wasatch Fault (WF) scenario simulations by Roten et al. (2011) in an updated WF Community Velocity Model (WFCVM-v3d) for the Salt Lake City segment that corrects artifacts in the velocity distribution near borehole locations (WFCVM-v3c, see Figure 1). In addition, we have simulated visco-elastic rupture and wave propagation in a 1D rock model selected to be the WFCVM-v3d velocity-density values at the location -111.73070526° , 40.57409668° , which is marked by the star in the right panel of Figure 1. The 1D rock model (Figure 2) has constant depths to velocity isosurfaces and the same V_{s30} everywhere (1,444 m/s). Figure 3 shows a map of the Quaternary surface faulting on the Wasatch fault zone and the 3D structure of the WFSLC rupture model used in the M 7 earthquake simulations. The 1D simulations use the same source models (e.g., identical slip and peak slip rate distributions) used in the 3D simulations in Roten et al., 2011, and in this study. Since the 1D and 3D simulations used the same source models, the ground motion differences observed are due to differences in wave propagation effects that result primarily from the presence of the Salt Lake Basin in the WFCVM. The effects of the basin include amplification of seismic waves traveling into regions of lower seismic velocities within the basin, focusing and defocusing by non-planar impedance contrasts, resonances, entrapment of waves in the basin, and generation of surface waves along the edges of the basin.

Figures 4 to 9 show comparisons between the SA-2s and SA-3s in the 1D and 3D models. Also, shown in these figures are slip and peak slip rate values. Figure 10 shows V_{s30} values and depths to the $V_s=1.0$ km/s and 1.5 km/s isosurfaces for comparison with the SA-2s and SA-3s values. Notice that the ground motion intensities from the 1D model are generally smoother and smaller in amplitude due to the lack of underlying 3D structure and higher V_{s30} values. The ratios of 3D/1D SA values shown in Figures 4-9 illustrate the 3D basin effects in SLV, such as focusing, defocusing, and entrapment of waves in ‘pockets’ of the basin. Such effects are observed above the deeper parts of the basin for all scenarios, such as just SW of South Salt Lake for scenario A (particularly for SA-2s), and just northwest of downtown SLC for scenario A’, B and B’.

The isosurfaces of $V_s=1.0$ km/s and $V_s=1.5$ km/s show similar trends in the basin structure, namely the deepest part is just northwest of downtown SLC, with shallower sub-basins to the north of the Oquirrh Mountains and in the southern part of the Salt Lake Valley (near Midvale). The smallest V_{s30} values of ~ 200 m/s are located in the northern and east-central parts of the valley. The V_{s30} values are negatively correlated with the associated depth to the isosurfaces (e.g., smaller V_{s30} above larger depths to isosurfaces), but do not appear to be a good predictor of the areas of the largest long-period SA-3s and SA-2s values.

In order to quantify the correlation between the SAs and the basin structure, we calculated the 2D correlation coefficient (R) between the SA values from the six 3D simulations and the isosurface depths for $V_s=1.0$ km/s and 1.5 km/s as well as for V_{s30} (Figure 11). The correlation coefficients are very similar for SA-2s and SA-3s and the two isosurfaces, with the largest values obtained for scenarios B’, C and D (0.70-0.80) as compared to 0.60-0.68 for scenarios A, A’ and B. The SAs show expectedly a negative correlation with the V_{s30} distributions, with correlation coefficients between -0.33 and -0.57. Thus, the deep basin structure appears to be a slightly better estimator of amplification than V_{s30} at periods of 2 and 3 sec.

Figure 12 shows the average amplification effects derived from the 6-scenario ensemble of simulations, quantified as the mean 3D/1D ratio of SAs at periods of 3s and 2s, compared to the amplification factors from a representative NGA-West2 GMPE, Boore et al. (2014) (henceforth BSSA14). The BSSA14 amplification factors are functions of the variable depth to the $V_s=1.0$ km/s isosurface and V_{s30} in the model domain. In general, the BSSA14 amplification factors have a smoother spatial distribution (as expected), but are also larger than the corresponding values from the 6-scenario simulation means. For example, the range of the BSSA14 values in the deeper northeastern part of the valley is ~ 3.5 -5.5, but only ~ 2.5 -4.5 for the simulation ensemble. This discrepancy is even larger for the southwestern (shallower) part of the valley, where the range for the simulation ensemble is 0.5-2.5, and 1.5-3.5 for BSSA14, a discrepancy that is analyzed further later. In the next subsection, we provide a more comprehensive and quantitative comparison of the basin amplification factors derived from the simulations with those predicted by 4 NGA-West2 GMPEs.

Regression of Amplification with Basin Depth

We have developed a regression model for basin amplification in the SLV as a function of basin depth, similar to the approach used by Day et al. (2008) for southern California. We first bin the

depths (D) to a specified isosurface of V_s , either 1.0 km/s or 1.5 km/s. We define n_{bin} bins by specifying depths D_n^{bin} , $n = 1, \dots, n_{\text{bin}}$, at the bin centers, spaced at equal intervals $\Delta D = 100 \text{ m}$, and then form the binning matrix W ,

$$W_{nj} = \begin{cases} 1, & \text{if } (D_n^{\text{bin}} - \Delta D/2) \leq D_j \leq (D_n^{\text{bin}} + \Delta D/2) \\ 0, & \text{otherwise} \end{cases}$$

where D_j is the depth at site j . We calculate the source-averaged basin response factor for period T_m , $B(D_n, T_m)$, by taking the natural logarithm and averaging over all N_{site} sites (3,411,094) and over all $N_{\text{sn}} = 6$ scenarios. For the i th scenario and j th site, we compute the ratio $SA_{ij}^{3d}(T_m)/SA_{ij}^{1d}(T_m)$, where $SA_{ij}^{3d}(T_m)$ are the SAs using the 3-D WFCVM at period T_m and $SA_{ij}^{1d}(T_m)$ are the SAs using the 1-D velocity model at period T_m . The number of sites in the bins range between ~9,000 and 600,000.

$$B(D_n, T_m) = \left(N_{\text{sn}} \sum_{j=1}^{N_{\text{site}}} W_{nj} \right)^{-1} \sum_{i=1}^{N_{\text{sn}}} \sum_{j=1}^{N_{\text{site}}} W_{nj} \ln [SA_{ij}^{3d}(T_m)/SA_{ij}^{1d}(T_m)]$$

We use the approximate representation constructed by Day et al. (2008) to provide a simple functional form for representing basin effects in regression modeling of ground motion:

$$A(D, T) = a_0(T) + a_1(T)[1 - \exp(-D/300)] + a_2(T)[1 - \exp(-D/4000)]$$

where

$$a_i(T) = b_i + c_i T, \quad i = 0, 1, 2$$

with T given in seconds and D in meters.

The parameters b_i , c_i are calculated in a two-step procedure. Separate least squares fits (at each period T_m) of $A(D, T)$ to $B(D_n, T_m)$ provided individual estimates of the $a_i(T_m)$ values for each period T_m . Then parameters b_i and c_i , for $i = 0, 1, 2$ were obtained by least-squares fits of these individual $a_i(T_m)$ estimates (although with only two periods, the linear fits are unique for this application). The resulting values for $D = Z_{1.0}$ and $Z_{1.5}$ are shown in Table 1.

Table 1. Coefficients For Basin Amplification Factor (Equation 1).

Isosurface	b_0	b_1	b_2	c_0	c_1	c_2
$V_s=1.0 \text{ km/s}$	-0.9542	5.647	-23.48	0.1906	-1.781	10.82
$V_s=1.5 \text{ km/s}$	-0.229	0.983	1.214	-0.1846	0.214	0.016

The variances s^2 (s is standard deviation) of the logarithm of amplification as a function of depth and period are:

$$s^2(D_n, T_m) = \left(N_{sn} \sum_{j=1}^{N_{site}} W_{nj} \right)^{-1} \sum_{i=1}^{N_{sn}} \sum_{j=1}^{N_{site}} W_{nj} \{ \ln[SA_{ij}^{3d}(T_m)/SA_{ij}^{1d}(T_m)] - B(D_n, T_m) \}^2$$

Figure 13 shows the regression results for the natural log of amplification in the simulations as a function of the depth to the $V_s=1.0$ km/s and $V_s=1.5$ km/s isosurfaces. The regression for $V_s=1.5$ km/s shows similar amplification factors up to ~ 3.15 ($\ln[\text{Amp}] \sim 1.15$) at depths of ~ 1.2 km/s for both SA-3s and SA-2s, with small de-amplification for depths less than ~ 150 m (SA-2s) and ~ 180 m (SA-3s). For $V_s=1.0$ km/s, the regressions for SA-2s and SA-3s show larger differences, with larger amplifications for SA-2s than SA-3s for depths < 500 m. The largest depth of 680 m shows amplifications of ~ 2.7 for SA-2s and ~ 3.7 for SA-3s.

To compare the basin depth amplification factors from four selected NGA-West2 GMPEs, we did the same regressions for the GMPEs as a function of the depth to the $V_s=1.0$ km/s isosurface, Z1.0. Figure 14 shows the regression results for the natural log of amplification as a function of the depth to the $V_s=1.0$ km/s isosurface for BSSA14. Figures 15 and 16 show the regression results for the simulations and the four selected GMPEs: BSSA14 (Boore et al., 2014), ASK14 (Abrahamson et al., 2014), CB14 (Campbell and Bozorgnia, 2014), and CY14 (Chiou and Youngs, 2014). Table 2 lists the average amplification factors over the whole range of the depth to the $V_s=1.0$ km/s isosurface used in the regressions. The average 3D/1D amplification values for the GMPEs are much larger than those for the simulations. The GMPE overestimation of the amplification factors appears to be due primarily to inadequacies in the GMPE V_s30 scaling, most likely for the very high V_s30 value of 1,444 m/s in the 1D model. For this reason, we show an additional set of plots (Figures 17 and 18) with the GMPE regression curves normalized to 1 (natural log = 0) at $Z1.0 = 0$ m. With this normalization, it can be seen that the variation of the basin amplification with Z1.0 in the simulations is matched fairly well by three of the four GMPEs (CY14, ASK14, and BSSA14). Only CB14 shows a significantly different trend, namely a slower increase in amplification with depth. The relatively poor fit for CB14 is not surprising, because CB14 parameterizes basin depth with the depth to the $V_s=2.5$ km/s isosurface, Z2.5, whereas the other three GMPEs all parameterize basin depth with Z1.0.

Table 2. Average Amplification Factors from Regressions vs. Depth to $V_s=1.0$ km/s

Average Amp	Simulation	BSSA14	ASK14	CB14	CY14
2s	0.6920	1.2164	1.0793	1.4010	1.4137
3s	0.6754	1.1270	0.9527	1.4019	1.4236

Source Effects on Ground Motions

Effects of Source Descriptions

Above, we have examined correlations of the ground motion distributions with depth measurements of the basin and V_s30 values for the SLV. Another factor strongly affecting ground motion patterns is the source description associated with the M7 WF scenario events. Here, we consider significant source parameters such as distributions of slip and peak slip

velocity. In addition, rupture direction/hypocentral location is an important parameter that controls directivity, another possible factor in the final distribution of ground motions.

The first two panels in the bottom row of Figures 4-9 show the distributions of slip and peak slip rates for the scenarios. The largest asperities (defined as the areas of largest slip) tend to be located laterally opposite to and shallower than the hypocentral location for the unilateral ruptures (A, A', B, and B'), and updip from the hypocenters of the bilateral ruptures (C, D). There appears to be a correlation between the areas of the largest SA values for both the 3D and 1D simulations, and the immediately underlying slip concentrations. Examples include the southeastern part of the valley for scenarios A and B, and the east-central part of the valley for scenarios A' and D. However, there are also several cases where the largest ground motions are located above areas of limited slip, such as above the northern corner of the rupture (north of Salt Lake City) for scenarios B', and D. The range of correlation coefficients between the distributions of SAs and the underlying slip distributions is 0.70-0.87 in 3D and 0.55-0.82 in 1D (Figure 11). The correlation between peak slip rates and associated SAs in the valley immediately above is weaker, with the largest peak slip rates typically located at the edges of the asperities and/or the fault break, and near the hypocenter. The range of correlation coefficients between the distributions of SAs and the underlying peak slip rate distributions is 0.55-0.79 in 3D and 0.41-0.76 in 1D. The generally larger correlations between SAs and the underlying slip distributions in the 3D model suggest a possible enhancement of source effects by basin structure.

Rupture Direction Effects

Somerville et al. (1997) developed a (now widely used) directivity model dependent on the angle between the direction of rupture propagation and the direction of waves traveling from the fault to the site, and the fraction of the fault rupture surface that lies between the hypocenter and the site. Abrahamson (2000) modified the Somerville et al. model by adding distance and magnitude tapers. Bayless and Somerville (2013) further developed the model by removing normalization to the rupture length, using a different dependence on site azimuth, introducing azimuth tapers for dip-slip faults, and providing an extension of the model for geometrically complex faults. For dip-slip faults the Bayless and Somerville (2013) model, like the Somerville et al. (1997) model, considers only directivity effects from the updip component of the rupture propagation.

Here, we apply the directivity model of Bayless and Somerville (2013) for multi-section ("multi-segment") faults to quantify its effect on GMPE predictions of ground-motion SAs in the Wasatch fault zone. We considered three rupture models, which divide the fault into one, two, and ten sections along strike (Figure 19). The scenario hypocenter becomes the rupture initiation point on the first section. Following the Bayless and Somerville (2013) model, 'pseudo-hypocenters' for the rupture of successive sections are defined as the point on the edge of the fault section that is closest to the edge of the neighboring section, half way between the top and bottom of the rupture. The directivity adjustment term f_D for each section of a dip-slip fault is expressed as:

$$f_D = f_D(d, R_x, W, R_{rup}, M_w, A_z, T) = [C_0(T) + C_1(T) \ln(d) \cos(R_x/W)] T_{CD}(R_{rup}, W) T_{Mw}(M_w) T_{Az}(A_z),$$

where C_0 and C_1 are period (T) dependent coefficients, d is the width in km of the (dipping) fault section rupturing updip towards a site (minimum = 1 km and maximum = W ; see also Somerville et al., 1997), R_x is the horizontal distance from the top edge of the rupture measured perpendicular to the rupture strike, T_{CD} is a distance taper, R_{rup} is the closest distance to the fault rupture plane, W is the fault width, T_{Mw} is a magnitude taper, M_w is the moment magnitude of the earthquake (not the section), $T_{Az} = \sin^2(|A_z|)$ is an azimuth taper, and A_z is the NGA-defined source-to-site azimuth. The NGA azimuth is measured from the strike direction of the site's closest point on the surface projection of the top edge of the rupture (Ancheta et al., 2013). This azimuth, d , and R_{rup} are measured from each rupture section to the site whereas R_x is measured from the closest rupture section to the site (Jeffrey R. Bayless, written communication, January 27, 2017). The total directivity adjustment term f_D is a weighted average of the segments' directivity adjustment terms, with the seismic moments of the individual segments as the weights. We modified the median spectral acceleration SA_{med} from four leading NGA-West2 GMPEs (calculated without directivity effects) to include f_D by setting $SA_{dir} = SA_{med} e^{f_D}$.

Maps of the directivity factors e^{f_D} for scenarios A and C at 2s and 3s periods are shown in Figures 20 and 21. It is evident that the Bayless and Somerville (2013) directivity factors depend strongly on how the fault plane is subdivided into segments, generally producing smaller directivity factors with a larger number of segments. Here, we apply the factors with the 1-segment WFSLC approximation to the GMPEs to estimate the largest possible directivity effects from the model. Figures 22-25 show comparisons between SAs from 3D and 1D simulations for scenarios A and C to SAs predicted for the 3D model from the four selected NGA-West2 GMPEs, shown with and without the directivity factors from Bayless and Somerville (2013). It is clear that the largest effect of the directivity factors is to increase the ground motions almost uniformly next to the fault. These directivity factors do little to increase the similarity between the SAs from the GMPEs and the simulations because the rupture direction effects in the simulations vary strongly with distance along the fault. The directivity factors improve the match between the GMPEs and the simulations in only four of the eight cases examined for rupture scenario A (Figures 22 and 23) and only three of the eight cases examined for rupture scenario C (Figures 24 and 25).

Distance Dependence of the Ground Motions.

Roten et al. (2011) compared mean simulated 3s-SAs and 2s-SAs and the values from the NGA08 ground motion prediction equations CB08 (Campbell and Bozorgnia, 2008), AS08 (Abrahamson and Silva, 2008), and CY08 (Chiou and Youngs, 2008) as a function of R_{rup} . For sites on the hanging wall at rupture distances larger than ~ 4 km, the average simulated SAs were below the values predicted by all three NGA models. At $R_{rup} = 10$ km, the simulated 3s-SAs and 2s-SAs dropped below one standard deviation of the NGA predictions. In contrast, simulated long-period SAs on the footwall did not show such discrepancies with the NGA08 relations.

The bias between the simulated 3D SA distributions (geometric mean of six scenarios calculated in the WFCVM) and predicted SA distributions from 4 NGA-West2 GMPEs is shown by the maps in Figures 26-27 (3s) and 28-29 (2s), and as a function of R_{rup} in Figures 30 (3s) and 31 (2s) for soil and rock sites separately. All of the bias values are normalized by the standard deviations, σ , which range from ~ 0.67 to ~ 0.74 in natural log units. Because the bias is fairly

constant in all of the GMPEs (within $\pm 5\%$), the apparent distance dependences of the biases are not significantly affected by the normalization with the standard deviation. Comparisons for SAs calculated in the 1D model are shown as maps in Figures 32-33 (3s) and 34-35 (2s), and as a function of R_{rup} in Figures 36 (3s) and 37 (2s). Although all sites are rock sites in the 1D model, the sites are subdivided into soil or rock sites according to their 3D model classification to facilitate comparisons with the 3D results. In the 3D model, the soil sites ($V_{s30} < 750$ m/s) are primarily located on the hanging wall, whereas the rock sites ($V_{s30} > 750$ m/s) are located on both the footwall and the hanging wall in the mountain ranges surrounding the Salt Lake Valley (Figure 1).

Three pervasive distance trends are seen in the bias plots (Figures 30, 31, 36, and 37). The first trend is a gradual increase in bias from $R_{rup}=0$ to 1-1.5 km for all soil sites at 2s and 3s in both models, about twice as large in the 3D as compared to the 1D results. An increase in bias from $R_{rup}=0$ to ~ 0.25 km for all rock sites is also seen at 2s and 3s in both 1D and 3D models. The second trend is a decrease in bias from $R_{rup} \sim 4$ km to ~ 10 km for all soil sites at 2s and 3s in both models, again about twice as large in the 3D results as in the 1D results. The result of these two trends is a relative high in the bias plots for $R_{rup} \sim 1-4$ km on the hanging wall side of the fault, which is also evident in maps of geometric mean SAs from the six different scenarios (Figure 38). O'Connell et al. (2007) found a similar pattern for 3D simulations of large earthquakes on the Teton fault where the highest peak ground velocities (PGVs) occurred at distances of 1-4 km from the surface trace of the fault, also on the hanging wall side. The third pervasive trend consists of an increase in bias for soil sites for both 2s and 3s SAs as R_{rup} increases from ~ 12 to 20 km, with the amount of increase comparable for both the 1D and 3D models.

Because trend 1 is more pronounced in the 3D simulations, we interpret it as partly caused by the basin edge effect, as hypothesized by Roten et al. (2011). The basin edge effect is caused by constructive interference between basin-edge-generated surface waves and the direct S wave (e.g., Kawase, 1996; Pitarka et al., 1998), and is only present in the 3D model. Because a positive bias near the fault occurs also in the 1D models, entrapment of waves by the horizontally layered structure may also be contributing to this amplification. Alternatively, the drop-off of the bias in SAs at distances less than 1.5 km from the fault trace could be related to velocity strengthening fault friction in the shallow part of the fault. Shallow velocity strengthening was emulated in the dynamic rupture simulations performed by Roten et al. (2011) in order to produce realistic ground motions, and consequently affects both the 3D and 1D simulations. The lower bias for near-fault rock sites is likely also caused by this source effect, but in a narrower zone because the fault dips below the valley sediments.

The gradual decrease in the bias for soil sites in the 3D model at distances of $\sim 4-10$ km (trend 2) was previously noted by Roten et al. (2011) for the 2008 NGA-West1 relations. This decrease is evident for the 2014 GMPEs as well and is most pronounced for BSSA14 and CB14 and smallest in size for CY14 (Figures 30 and 31). In comparison, the 2014 GMPEs for rock sites generally show little to no change in the bias at these distances from the fault. For this reason, we interpret this trend to be at least in part due to the basin effects discussed previously, as well as directivity effects. Another possible cause of this trend is the westward termination of the WF as well as associated significant slip in the M7 scenarios. While the nature of the GMPEs imply a smooth

distribution of slip on the fault, our scenarios produced the majority of the slip on the upper half of the fault, likely concentrating the highest ground motion amplitudes closer to the surface trace.

With trend 3 the bias increases with distance again at soil sites located within 12 to 20 km from the rupture (Figures 30 and 31). The bias maps for the 3D simulations (Figures 26-29) typically show the lowest values, generally between -0.5σ and -2σ , in the southwestern part of the SLB, roughly to the SW of a line connecting West Valley City to Draper. In the NW part of the SLB, towards the Great Salt Lake, the bias tends to range between $+0.5$ and -1σ . Therefore, we interpret trend 3 to be an artifact of the distribution of rupture distances in the basin in combination with azimuthal variations in ground motions. The apparent distance trend occurs because the distance range between 12 and 20 km includes more points from the NW part of the basin than from the SW part. (For a map with rupture distances, refer to Figure 9 in Roten et al., 2011).

The simulations in Roten et al. (2011) used the Q_s - V_s relation by Brocher (2006). In order to test whether a less attenuating Q distribution can account for the bias at $R_{rup} \sim 4$ -10 km, we simulated scenario A' using the relations $Q_s = 0.1 V_s$ (V_s in km/s) and $Q_p = 2 Q_s$ (based on results from Withers et al., 2015). The distributions of SA-2s for scenario A' simulated with the 2 different Q distributions are shown in Figure 39. The main differences between the SA-2s results are larger SA-2s values within ~ 10 km to the west of the fault trace, in particular N and NW of SLC. Figure 40 shows the bias relative to BSSA14 and CB14 of SA-2s from simulations with the two different Q relations, suggesting that the Brocher (2006) Q relation provides slightly greater overall similarity to the GMPEs.

Hanging Wall Effects

The ASK14, CB14, and CY14 GMPEs have explicit factors to account for observed systematic ground motion differences between sites on the hanging wall and footwall located at the same distance from the closest part of the rupture (e.g., Abrahamson and Somerville, 1996). These “hanging wall factors” are all based in part on finite fault simulations by Donahue and Abrahamson (2014). The expectation of higher ground motions on the hanging wall is implicit in the distance definition used in BSSA14, which is the closest horizontal distance to the surface projection of the rupture. Chiou et al. (1999a,b) and Donahue and Abrahamson (2014) showed that the larger ground motions at hanging wall sites could be explained as a geometrical effect resulting from the fact that the average distance to the rupture from a hanging wall site is less than that for a footwall site at the same closest distance. Note that this hanging wall effect is independent of, and in addition to, any ground motion amplifications that may be caused by low velocity sediments on the hanging wall.

The hanging wall factors in the 2008 and 2014 NGA equations are based primarily on data and simulations for reverse-faulting earthquakes. Consequently, the application of these hanging wall factors to normal-faulting earthquakes has been somewhat controversial. Here, we test the applicability of these factors to normal faulting earthquakes using the results of our simulations for the 1D rock model.

Figure 41 compares geometric mean SA-2s and SA-3s values from the six 1D simulations with GMPE predictions for sites within a 4-km-wide zone trending ENE-WSW across the center of the simulated WFSLC rupture. The horizontal axis in Figure 41 is R_x , the horizontal distance from the top of the rupture measured perpendicular to strike. R_x is defined as positive on the hanging wall side. All of the SAs shown are normalized to 1.0 at a footwall reference site where $R_x = -12.2$ km (40.7635° , -111.6972°). Each SA value plotted is a geometric mean for sites within a 1-km R_x bin

Figure 41 shows that the GMPEs do a reasonably good job of predicting the increased ground motions over the hanging wall for SA-3s, although the fit for BSSA14 is not as good as for the others. For SA-2s, the simulations show minimal increase over the hanging wall and the GMPEs overpredict the simulations. However, the overpredictions are less than 1 standard deviation except for BSSA14.

References

- Abrahamson, N.A. (2000). Effects of rupture directivity on probabilistic seismic hazard analysis, *Proceedings from the 6th International Conference on Seismic Zonation*, Palm Springs, California, *Earthq. Eng. Res. Inst. CD-2000-01*.
- Abrahamson, N., and W. Silva (2008). Summary of the Abrahamson & Silva NGA ground-motion relations, *Earthquake Spectra* **24**, no. 1, 67–97.
- Abrahamson, N.A., W.J. Silva, and R. Kamai (2014). Summary of the ASK14 ground motion relation for active crustal regions, *Earthquake Spectra* **30**, no. 3, 1025-1055.
- Abrahamson, N.A., and P.G. Somerville (1996). Effects of the hanging wall and footwall on ground motions recorded during the Northridge earthquake, *Bull. Seism. Soc. Am.* **86**, S93-S99.
- Ancheta, T.D., R.B. Darragh, J.P. Stewart, E. Seyhan, W.J. Silva, B.S.J. Chiou, K.E. Wooddell, R.W. Graves, A.R. Kottke, D.M. Boore, T. Kishida, and J.L. Donahue (2013). PEER NGA-West2 database, *Pacific Earthquake Engineering Center PEER Report 2013/03*, 134 pp.
- Bayless, J., and P. Somerville (2013). Bayless and Somerville model, Chapter 2 in *Final report of the NGA-West2 directivity working group*, P. Spudich (Editor), *Pacific Earthquake Engineering Research Center PEER Report 2013/09*, Berkeley, CA, 29-96.
- Boore, D.M., J.P. Stewart, E. Seyhan, and G.M. Atkinson (2014). NGA-West2 equations for predicting PGA, PGV, and 5% damped PSA for shallow crustal earthquakes, *Earthquake Spectra* **30**, no. 3, 1057-1085.
- Brocher, T. (2006). Key elements of regional seismic velocity models for ground motion simulations, in Proc. of Int. Workshop on Long-Period Ground Motion Simulations and Velocity Structures, Tokyo, Japan, 14–15 Nov.

- Campbell, K. W., and Y. Bozorgnia (2008). NGA ground motion model for the geometric mean horizontal component of PGA, PGV, PGD and 5% damped linear elastic response spectra for periods ranging from 0.01 to 10 s, *Earthquake Spectra* **24**, no. 1, 139–171.
- Campbell, K.W., and Y. Bozorgnia (2014). NGA-West2 ground motion model for the average horizontal components of PGA, PGV, and 5% damped linear acceleration response spectra, *Earthquake Spectra* **30**, no. 3, 1087-1115.
- Chiou, S.J., F. Makdisi, and R.R. Youngs (1999a). Style-of-faulting and footwall/hanging wall effects, *Seism. Res. Lett.* **70**, 216.
- Chiou, S.J., F. Makdisi, and R.R. Youngs (1999b). Style-of-faulting and footwall/hanging wall effects on strong ground motions, Final Technical Rept., U.S. Geol. Surv. Award No. 1434-95-G-2614, 21 pp.
- Chiou, B.S.J., and R.R. Youngs (2008). An NGA model for the average horizontal component of peak ground motion and response spectra, *Earthquake Spectra* **24**, no. 1, 173–215.
- Chiou, B.S.J., and R.R. Youngs (2014). Update of the Chiou and Youngs NGA model for the average horizontal component of peak ground motion and response spectra, *Earthquake Spectra* **30**, no. 3, 1117-1153.
- Day, S. M., R. W. Graves, J. Bielak, D. Dreger, S. Larsen, K. B. Olsen, A. Pitarka, and L. Ramirez-Guzman (2008). Model for basin effects on long-period response spectra in southern California, *Earthquake Spectra* **24**, 257-277.
- Donahue, D.L., and N.A. Abrahamson (2014). Simulation-based hanging wall effects, *Earthquake Spectra* **30**, no. 3, 1269-1284.
- Kawase, H. (1996). The cause of the damage belt in Kobe: "The basin-edge effect," constructive interference of the direct S-wave with the basin-induced diffracted/Rayleigh waves, *Seism. Res. Lett.* **67**, no. 5, 25-34.
- Pitarka, A., K. Irikura, T. Iwata, and H. Sekiguchi (1988). Three-dimensional simulation of the near-fault ground motion for the 1995 Hyogo-Ken Nanbu (Kobe), Japan, earthquake, *Bull. Seism. Soc. Am.* **88**, 428-440.
- Roten, D., K.B. Olsen, J.C. Pechmann, V.M. Cruz-Atienza, and H. Magistrale (2011). 3-D simulations of M 7 earthquakes on the Wasatch fault, Utah, Part I: Long-period (0-1 Hz) ground motions, *Bull. Seism. Soc. Am.* **101**, 2045-2063 [correction to the author list added in **102**, 453].
- Somerville, P.G., N.F. Smith, R.W. Graves, and N.A. Abrahamson (1997). Modification of empirical strong ground motion attenuation relations to include the amplitude and duration effects of rupture directivity, *Seism Res. Lett.* **68**, no. 1, 199-222.

Spudich, P., J.R. Bayless, J.W. Baker, B.S.J. Chiou, B. Rowshandel, S.K. Shahi, and P. Somerville (2013). Final report of the NGA-West2 directivity working group, Pacific Earthquake Engineering Research Center *PEER Report 2013/09*, 129 pp.

Withers, K.B., K.B. Olsen, and S.M. Day (2015). Memory-efficient simulations of frequency-dependent Q , *Bull. Seism. Soc. Am.* **105**, 3129-3142.

**Bibliography of Publications Resulting from
Work Performed Under the Award**

Wang, N., D. Roten, K.B. Olsen, and J. Pechmann (2017). Rupture direction, basin, and distance effects on ground motions from M7 earthquakes on the Salt Lake City segment of the Wasatch fault, Utah, *Seism. Res. Lett.* **87**, no. 5, 648 (abstract).

Version 3c

Version 3d

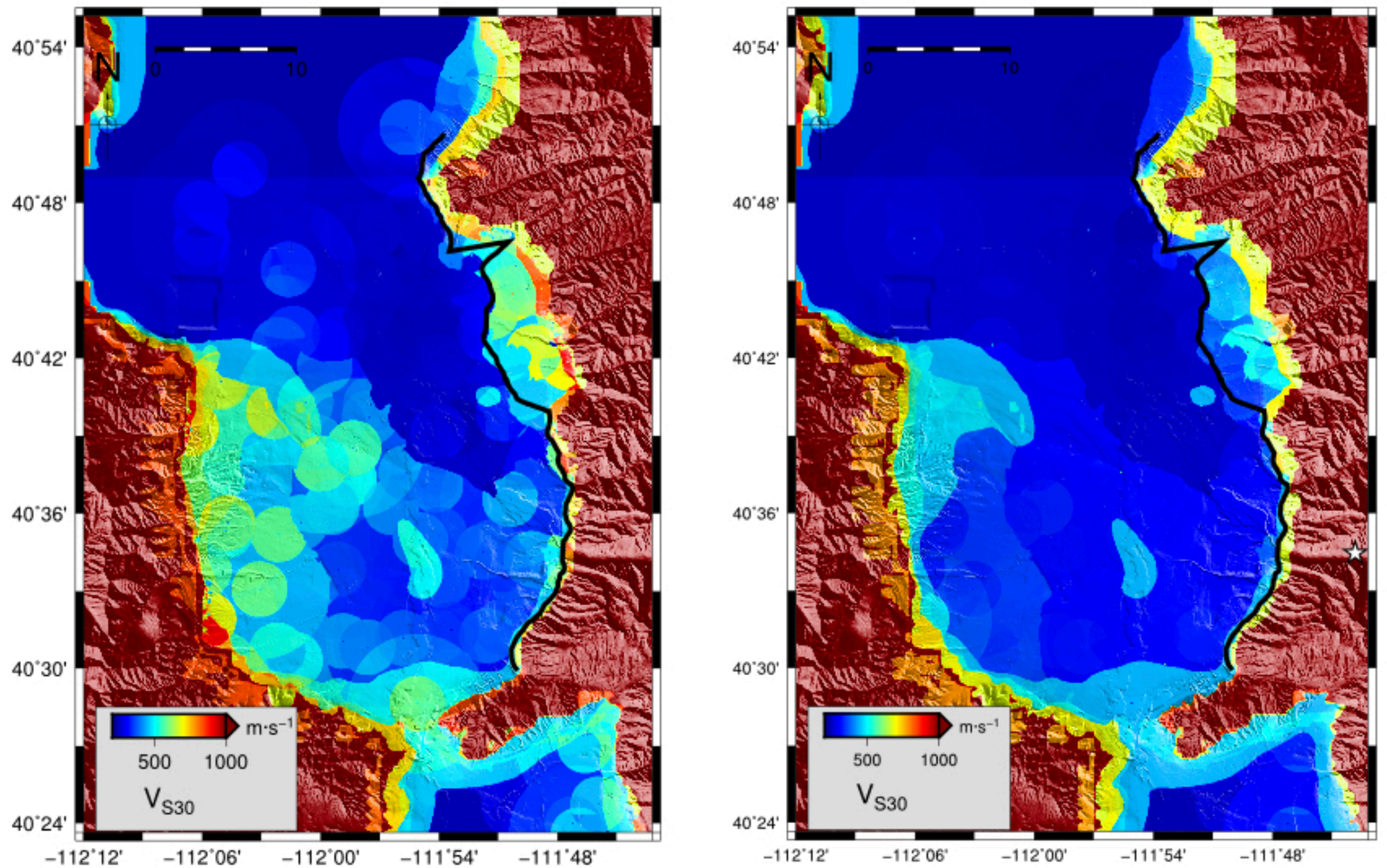


Figure 1. Distributions of V_{S30} for the WFCVM (left) version 3c and right (3d), interpolated from V_s values at zero and 40 m depth. The star shows the location where the 1D rock model is extracted. The black line depicts the WF surface trace.

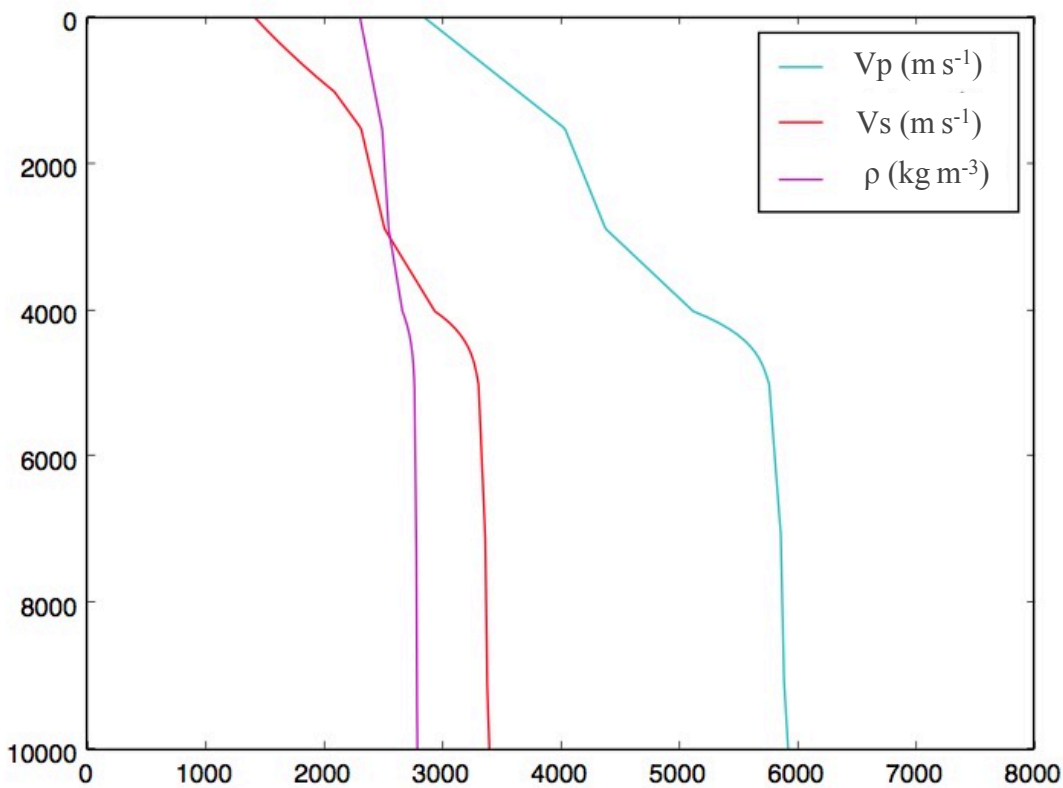


Figure 2. 1D rock model used for the 1D SLV simulations. V_p denotes P-wave velocity, V_s S-wave velocity, and ρ density. The V_{S30} value for this model is 1444 m/s.

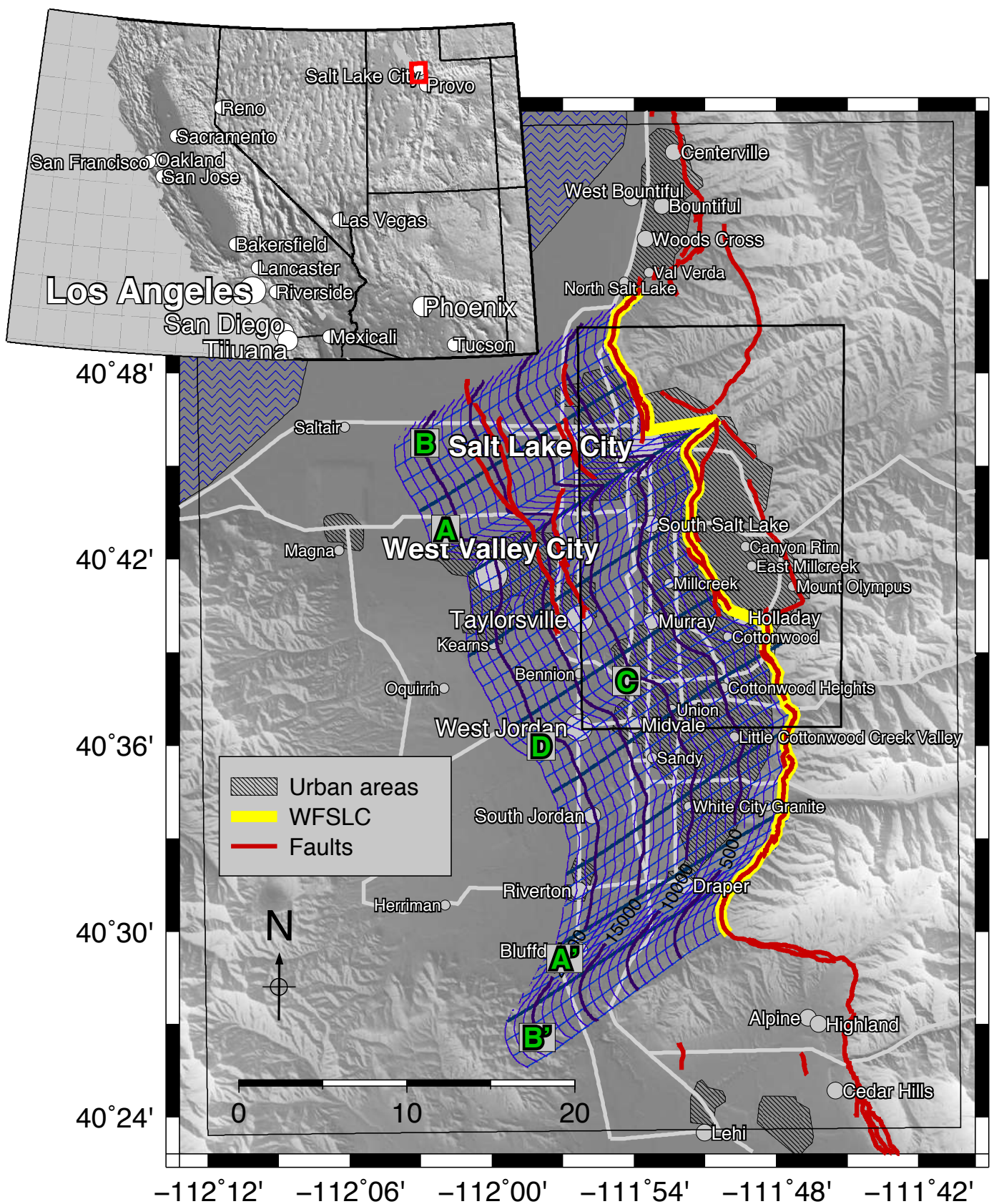


Figure 3. Map of the Salt Lake Basin showing known Quaternary surface faulting on the Wasatch fault zone and the surface trace of the WFSLC model. The mesh shows the 3D structure of the WFSLC with along-strike and along-dip distances in 1000 m contours. Letters represent the epicenter locations in the six rupture models. The outer rectangle shows the extent of the computational model used for the simulations (Roten et al., 2011).

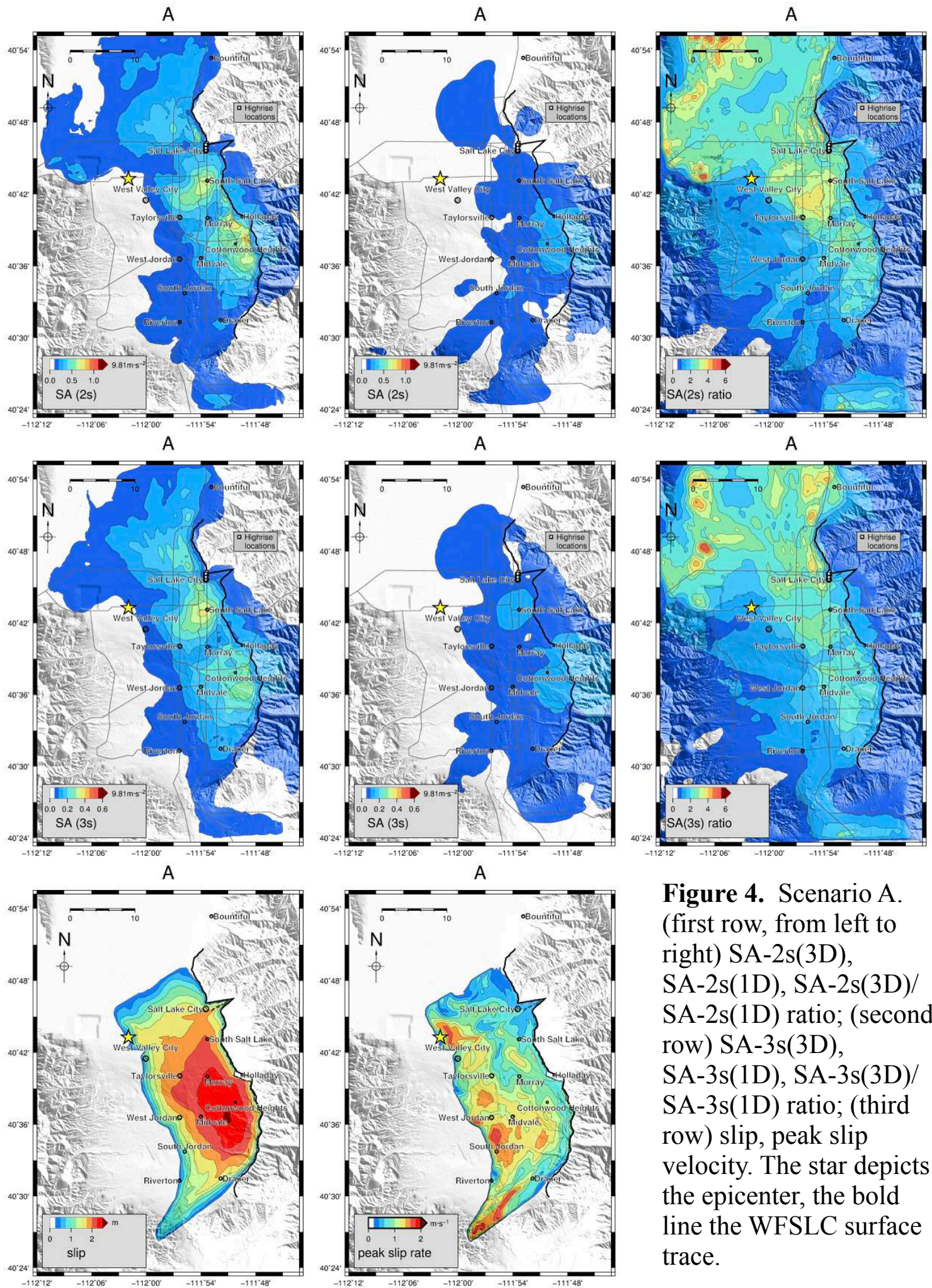


Figure 4. Scenario A. (first row, from left to right) SA-2s(3D), SA-2s(1D), SA-2s(3D)/SA-2s(1D) ratio; (second row) SA-3s(3D), SA-3s(1D), SA-3s(3D)/SA-3s(1D) ratio; (third row) slip, peak slip velocity. The star depicts the epicenter, the bold line the WFSLC surface trace.

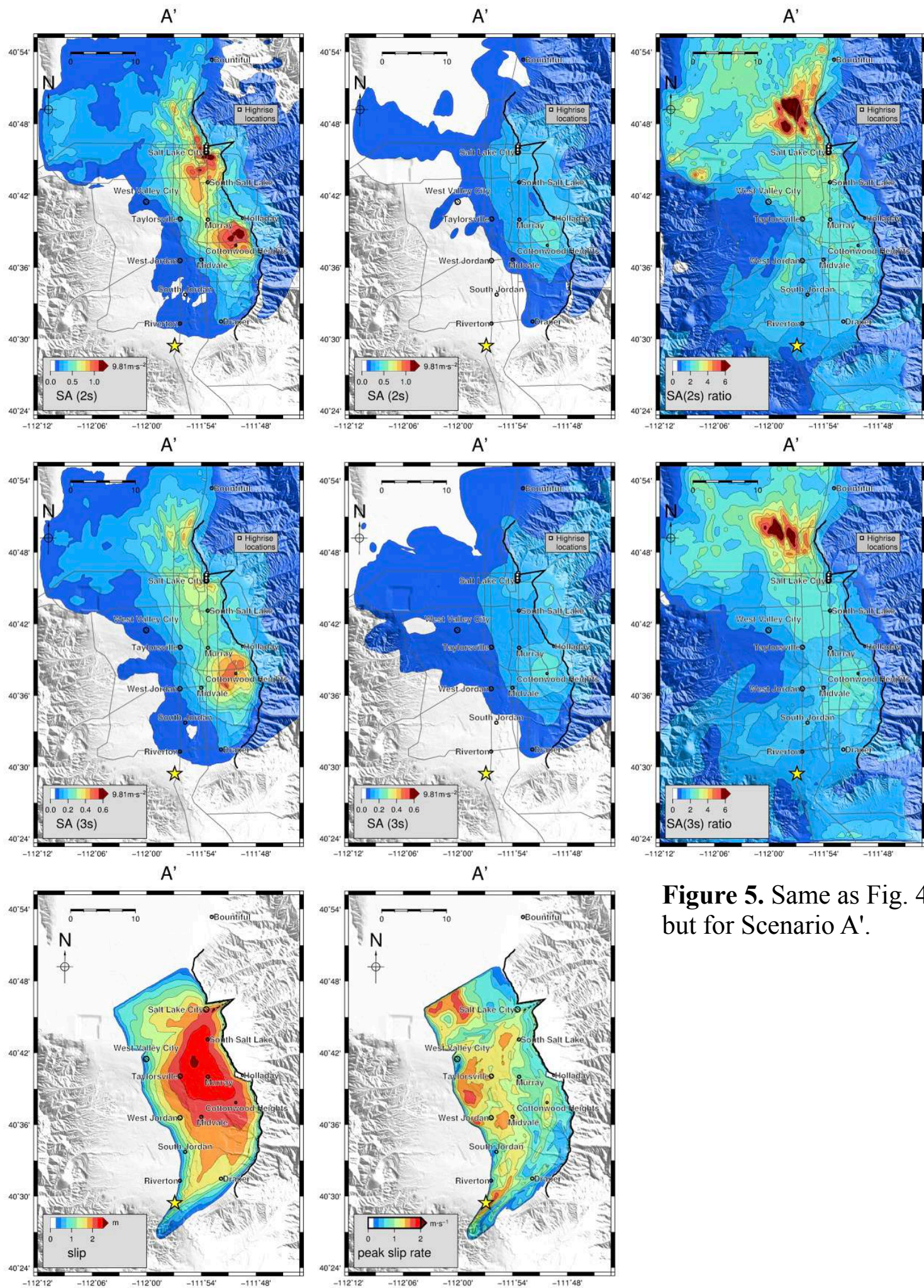


Figure 5. Same as Fig. 4, but for Scenario A'.

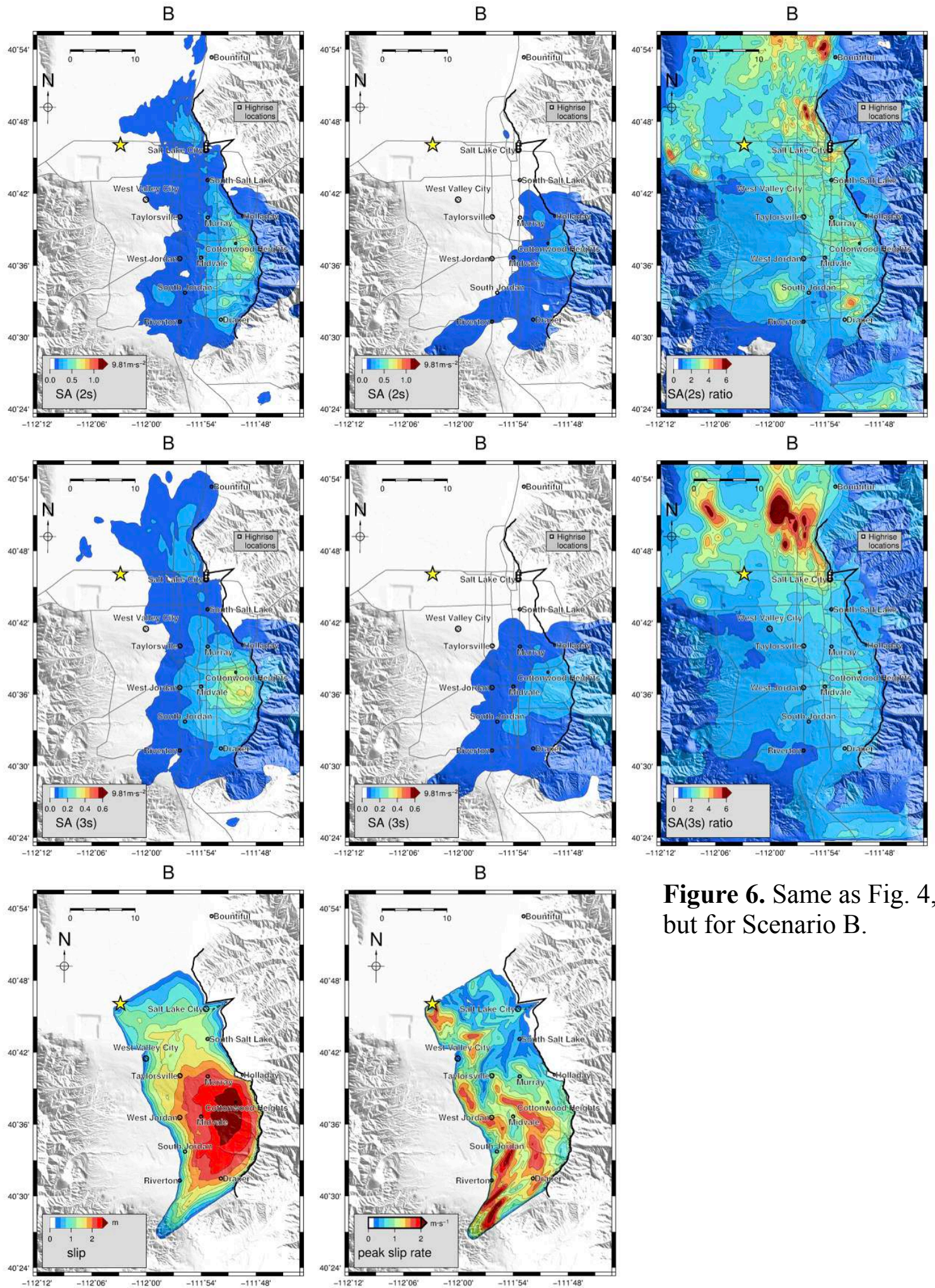


Figure 6. Same as Fig. 4, but for Scenario B.

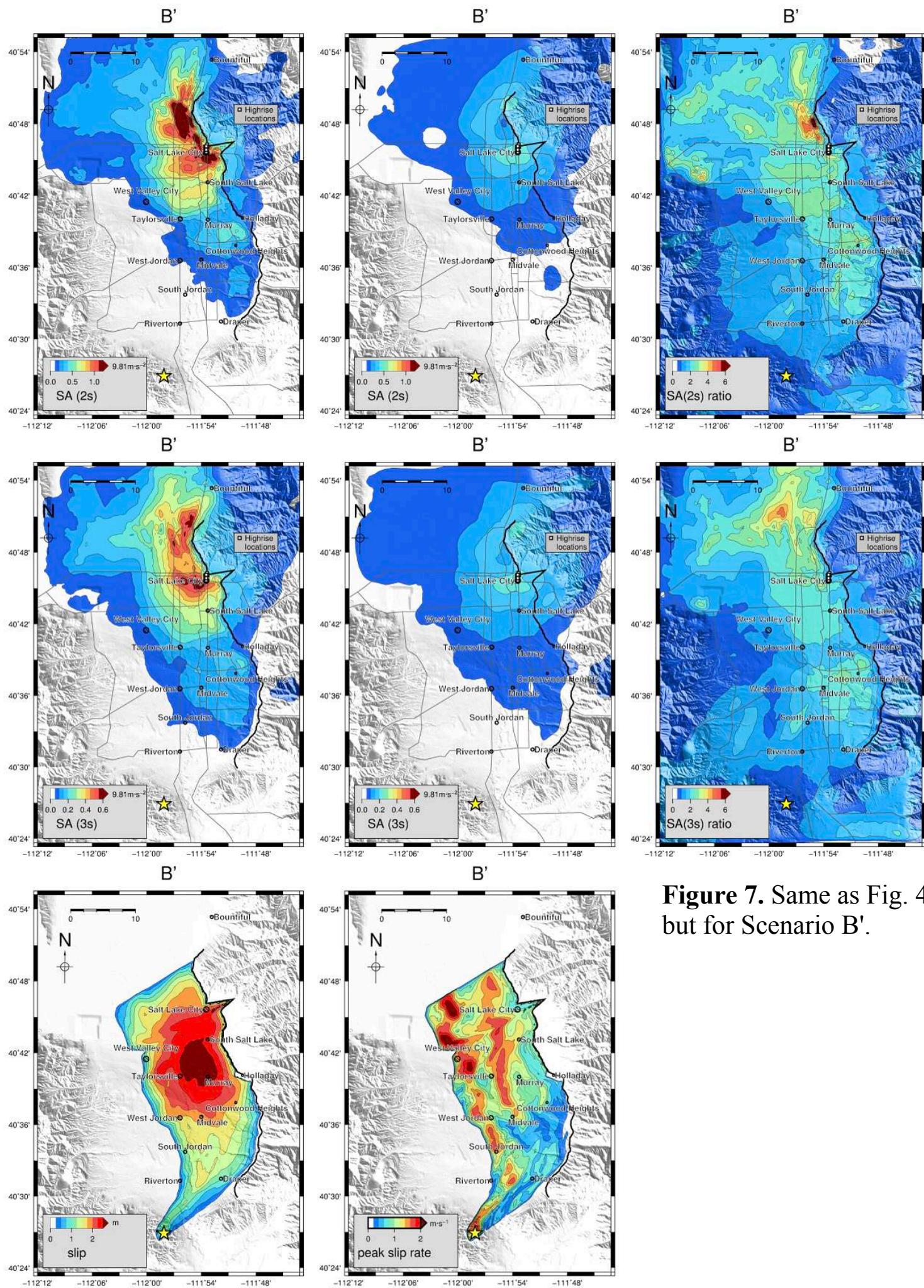


Figure 7. Same as Fig. 4, but for Scenario B'.

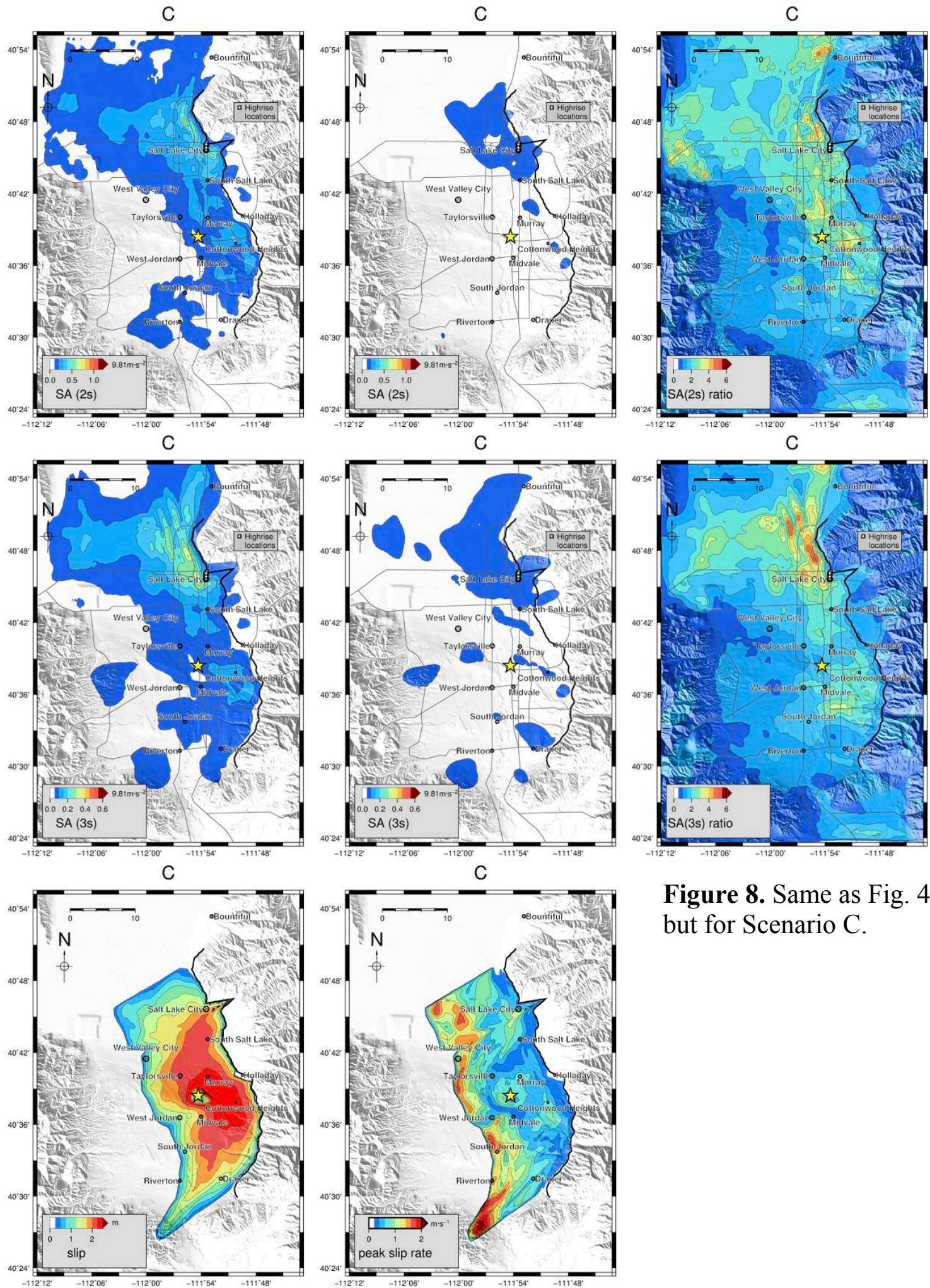


Figure 8. Same as Fig. 4, but for Scenario C.

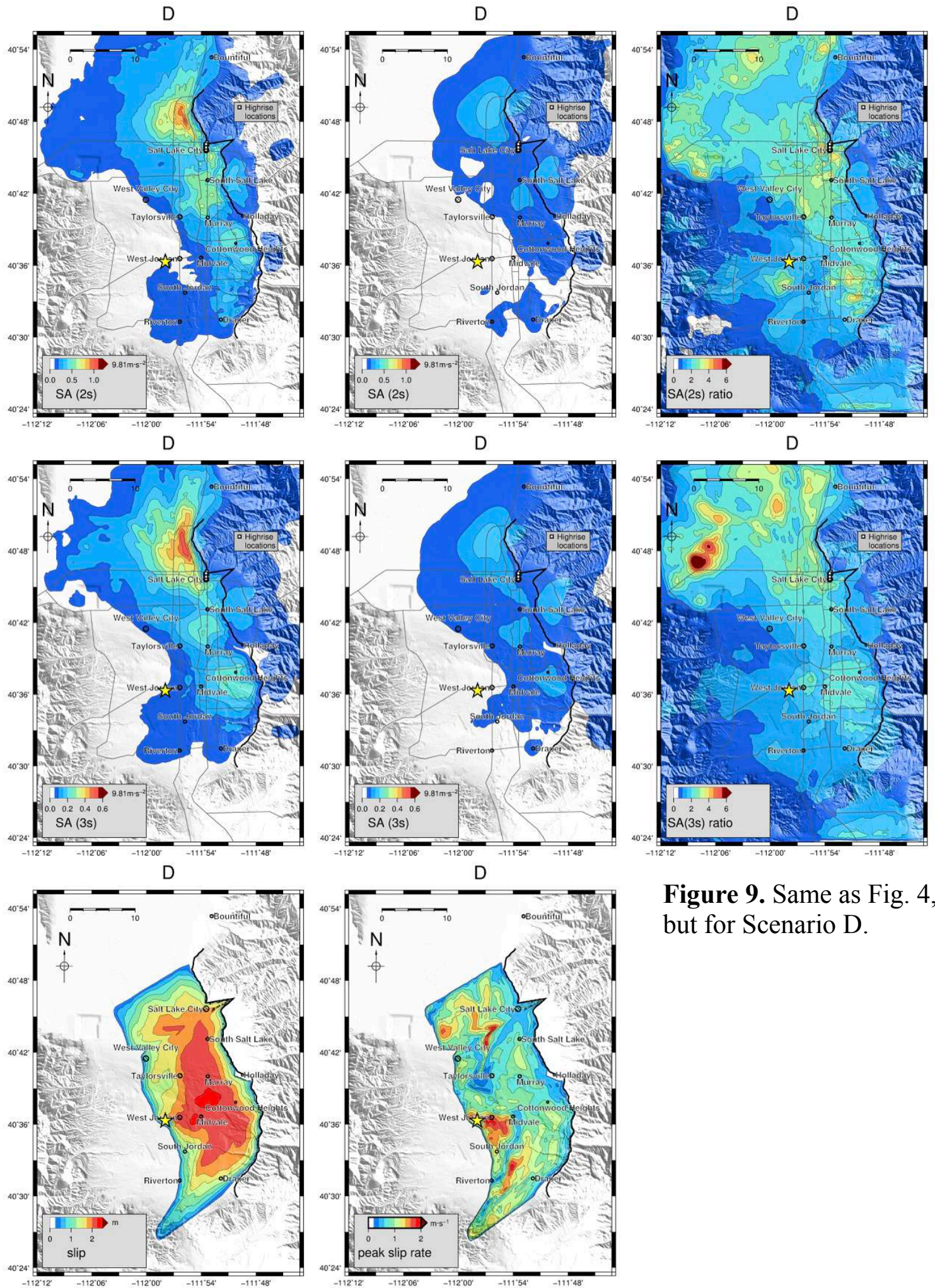


Figure 9. Same as Fig. 4, but for Scenario D.

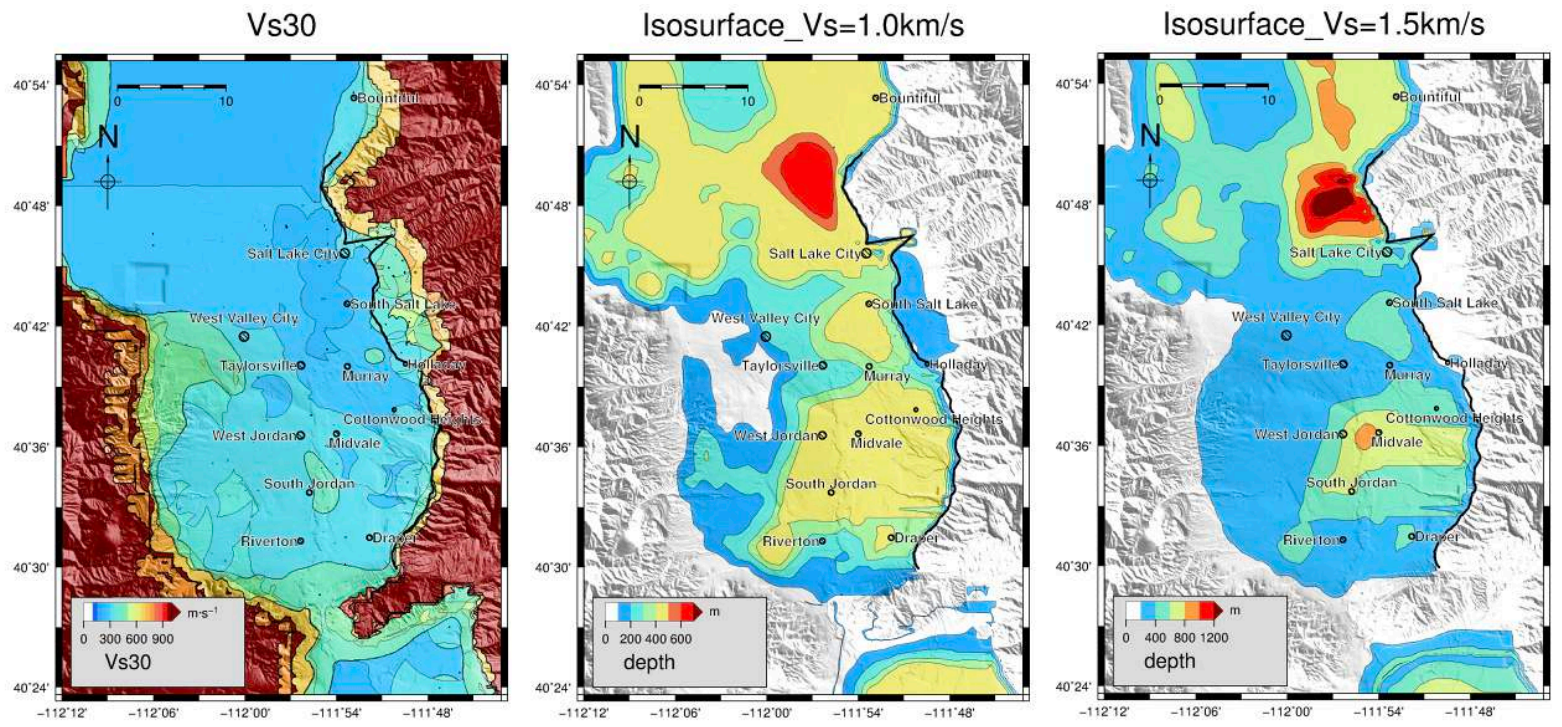


Figure 10. Distributions for the WFCVM of Vs30 (left), depth to Vs=1.0 km/s isosurface (middle), and depth to Vs=1.5 km/s isosurface (right). The bold line depicts the WFSLC surface trace.

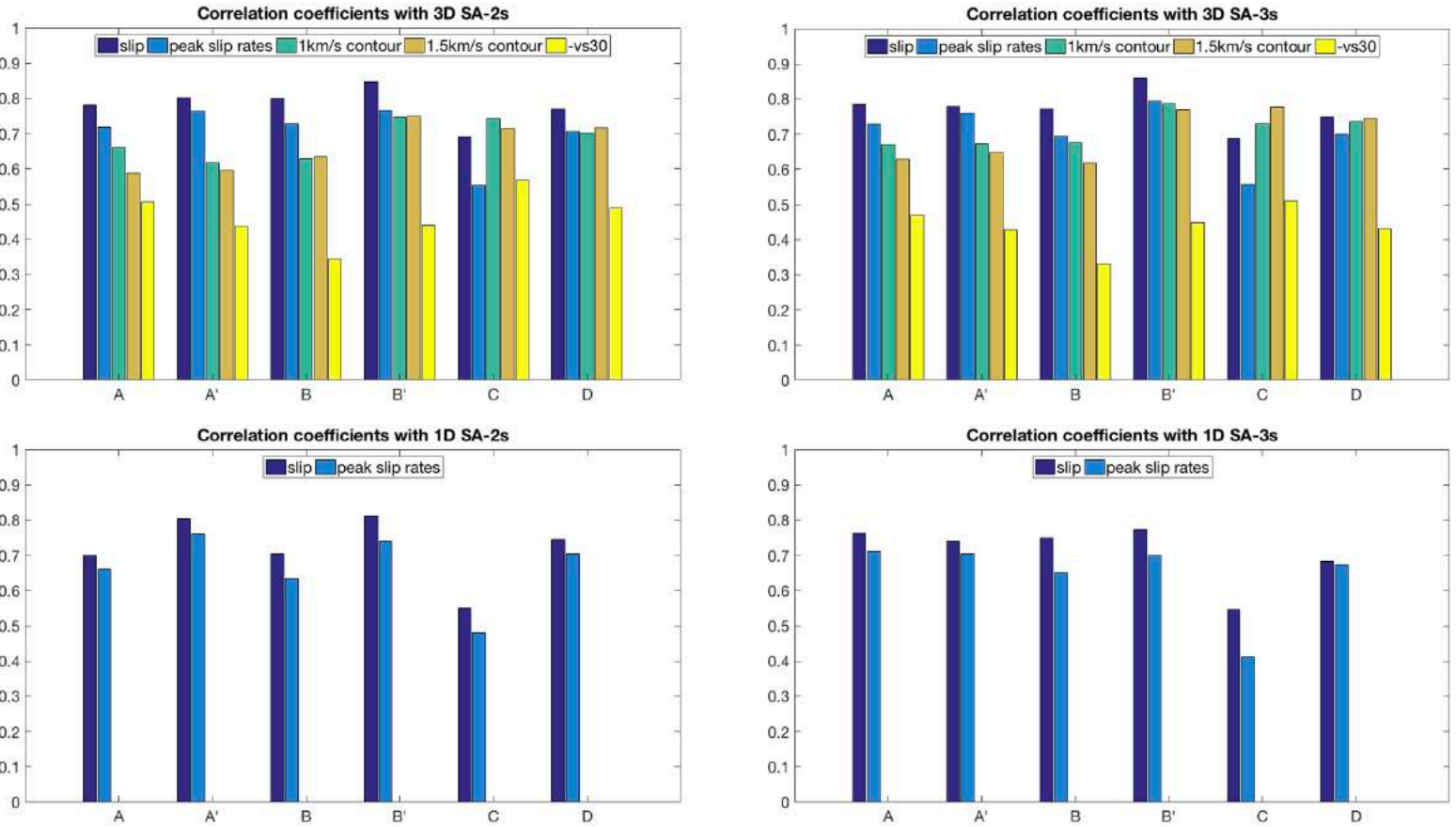


Figure 11. Correlation coefficients between the SA-2s (left) and SA-3s (right) values from the six scenarios and the distributions of slip, peak slip rate, depths to Vs=1.5 km/s and 1.0 km/s, and Vs30, for the simulations carried out in the (top) 3D WFCVM model and (bottom) 1D rock model.

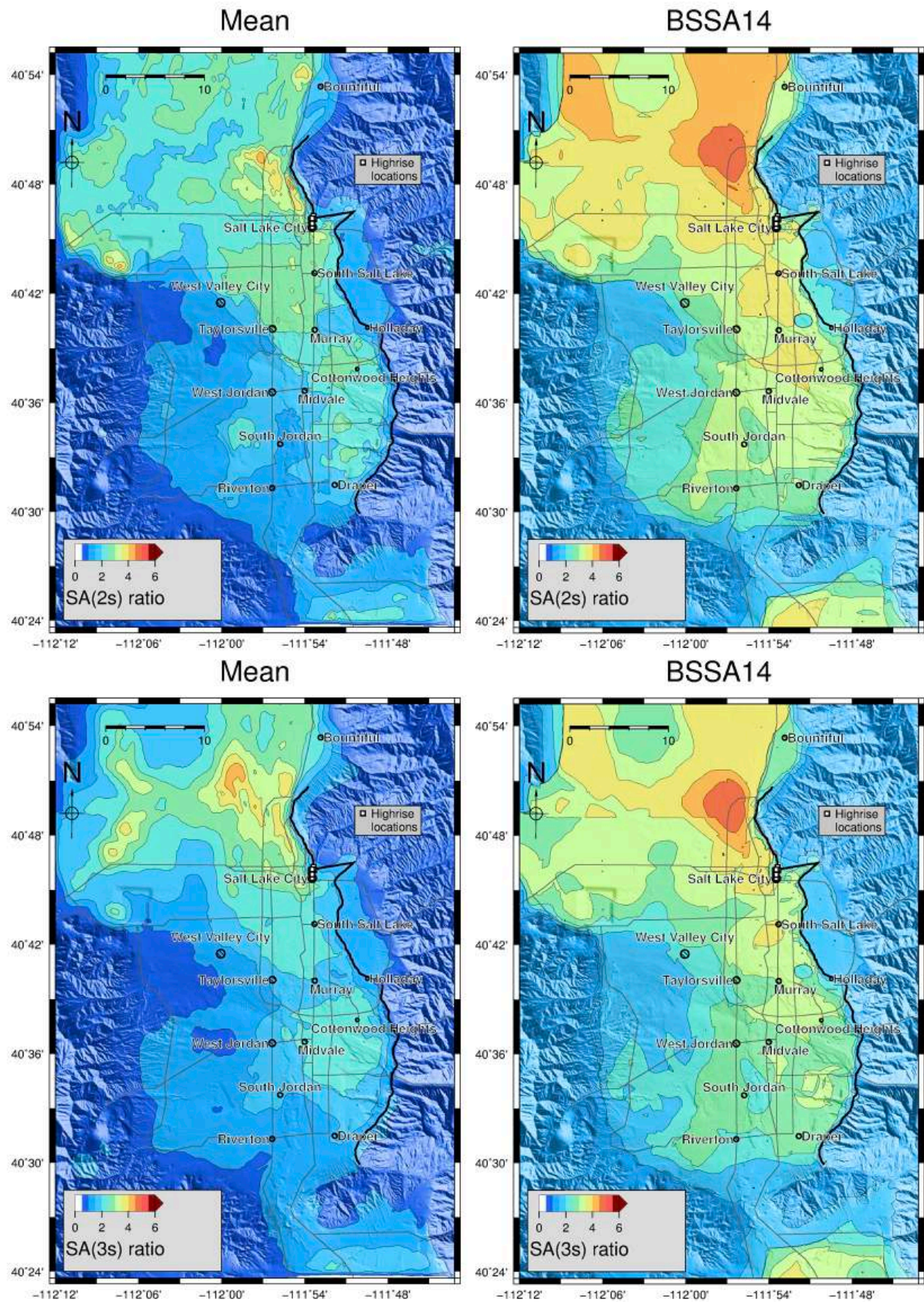


Figure 12. Maps of basin amplification for M7.0 Wasatch fault scenarios for (top) SA-2s and (bottom) SA-3s, from (left) 6-scenario average 3D/1D ratios and (right) the BSSA14 GMPE. The bold line depicts the WFSLC surface trace.

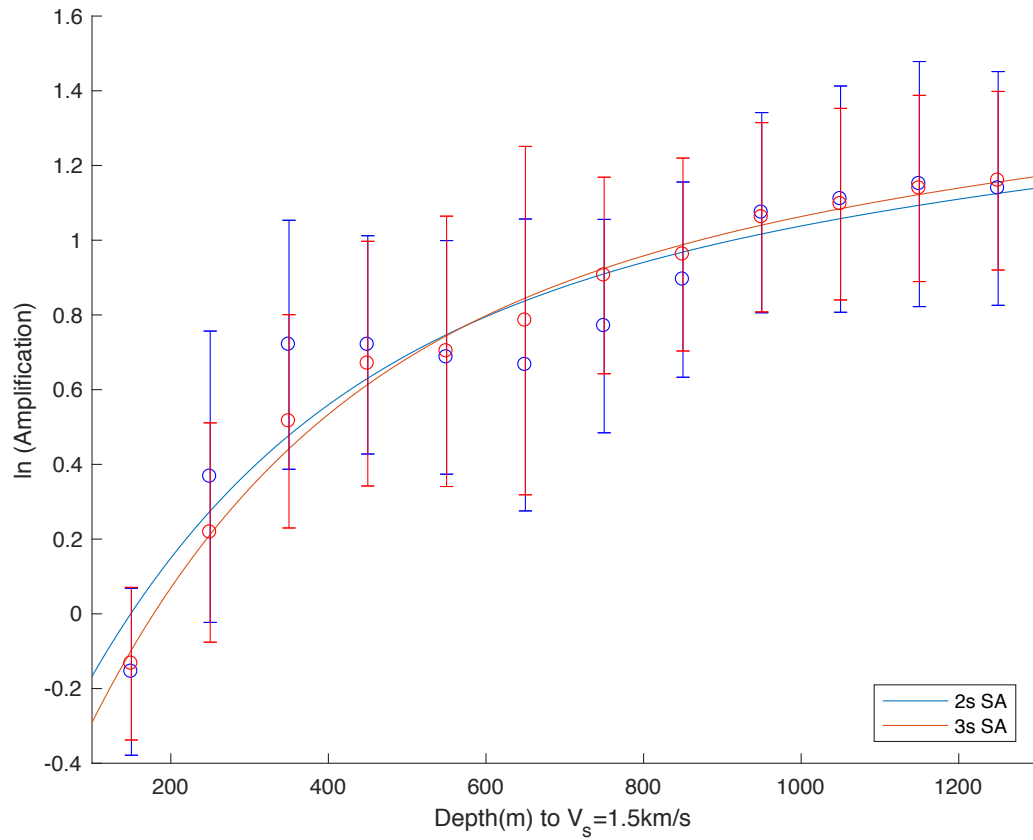
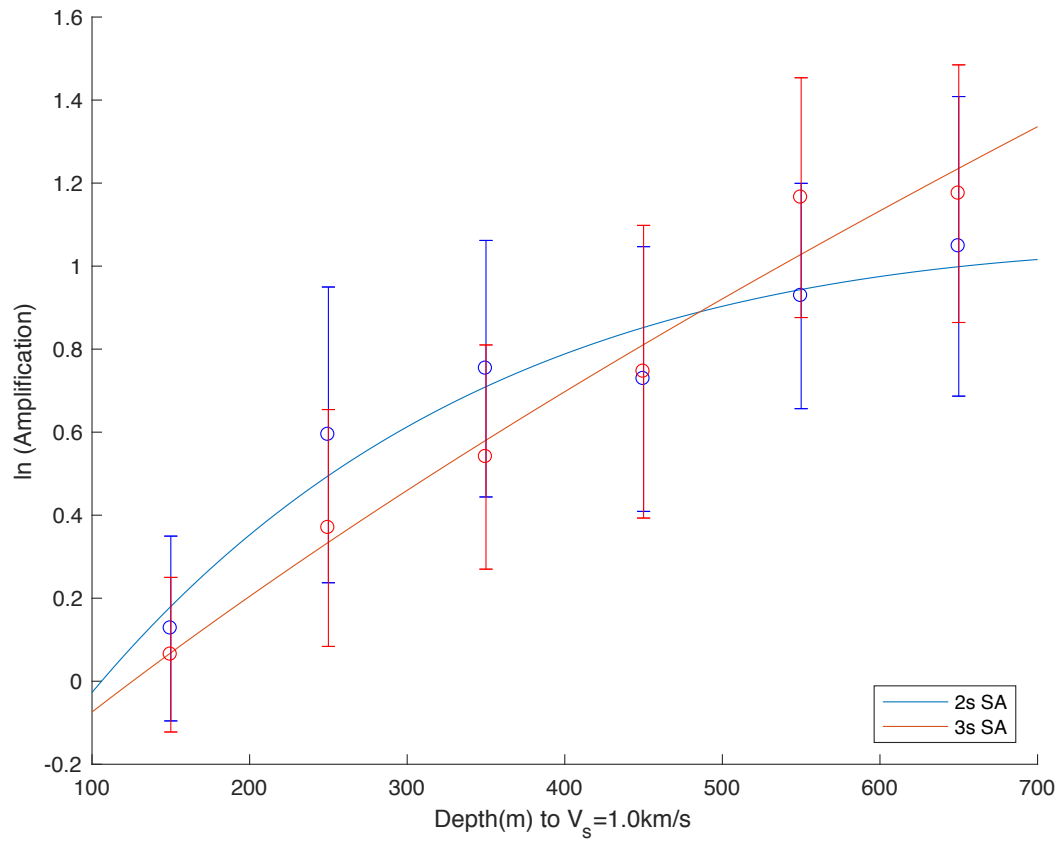


Figure 13. Natural log amplification factors as a function of depth to the isosurfaces of (top) $V_s = 1.0 \text{ km/s}$ and (bottom) $V_s = 1.5 \text{ km/s}$, for SA-2s (blue) and SA-3s (red). The circles depict the means for the depth bins (B), the error bars are the standard deviations, and the curved lines are the regression fits. The maximum isosurface depths in the study area are 680 m for $V_s = 1.0 \text{ km/s}$ and 1240 m for $V_s = 1.5 \text{ km/s}$.

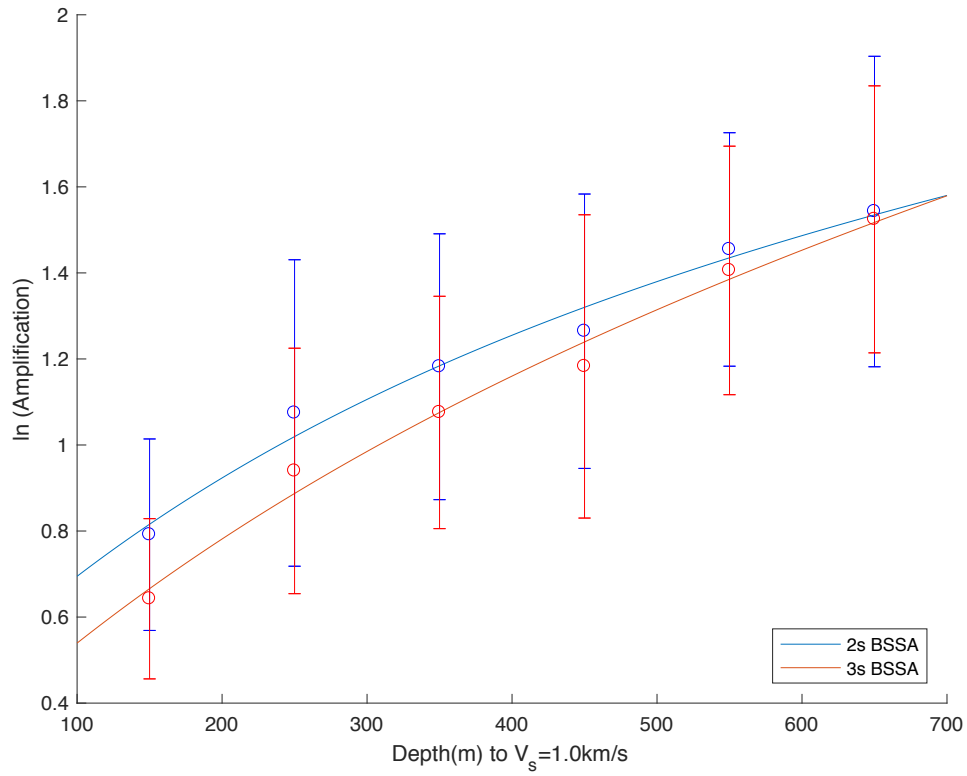


Figure 14. Natural log amplification factors as a function of depth to the isosurface of $V_s=1.0$ km/s, for BSSA14-2s (blue) and BSSA14-3s (red). The circles depict the means for the depth bins (B), the error bars are the standard deviations, and the curved lines are the regression fits.

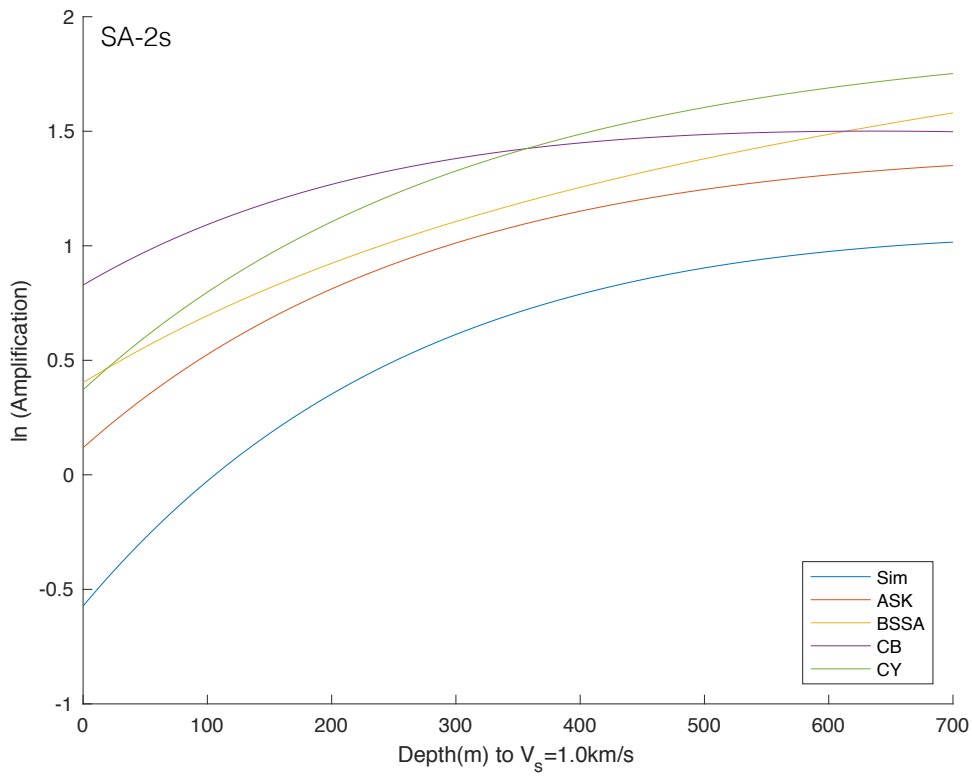


Figure 15. Comparison of the basin depth amplification factors regression results for 2s period from the GMPEs (ASK14, BSSA14, CB14, and CY14) to the regression results for the simulations (Sim).

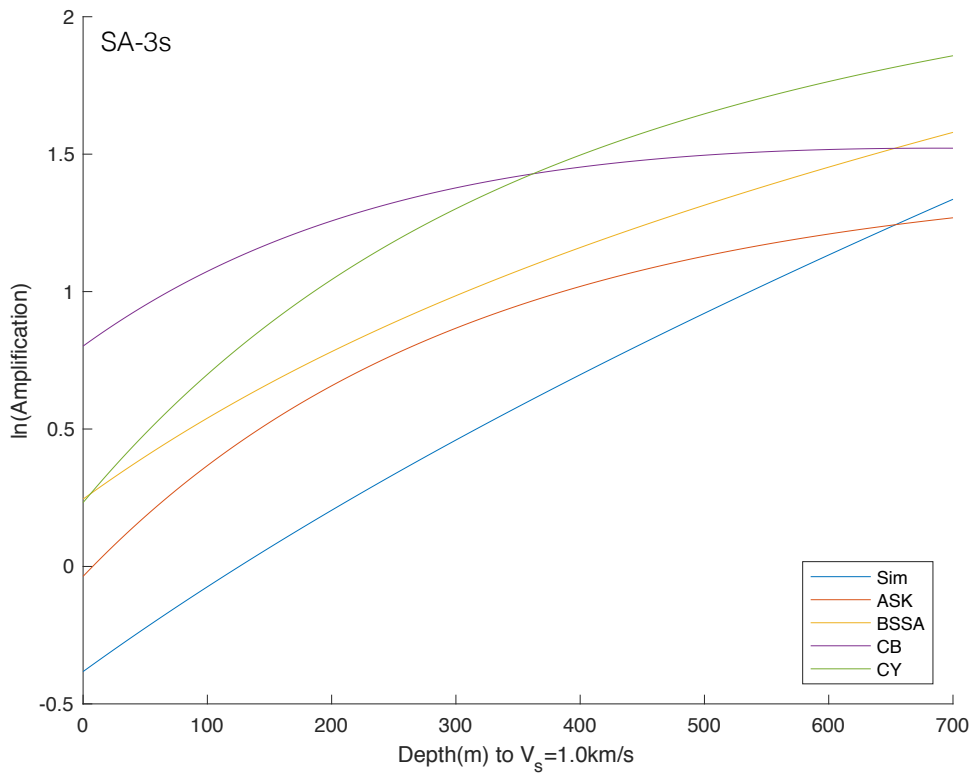


Figure 16. Comparison of the basin depth amplification factors regression results for 3s period from the GMPEs (ASK14, BSSA14, CB14, and CY14) to the regression results for the simulations (Sim).

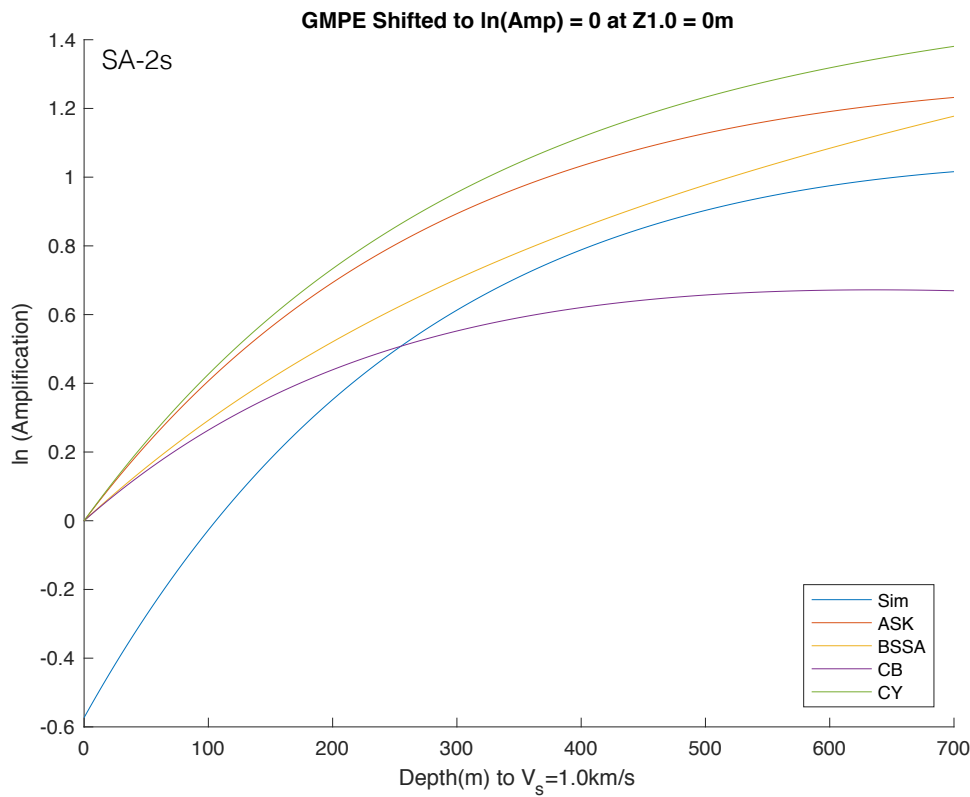


Figure 17. Comparison of the regression results for the basin depth amplification factors at a period of 2s from the GMPEs (ASK14, BSSA14, CB14, and CY14) to the results of the simulations (Sim). The GMPEs' regression curves are shifted to $\ln(\text{Amp})=0$ at a depth to the $V_s=1.0$ km/s isosurface of 0m.

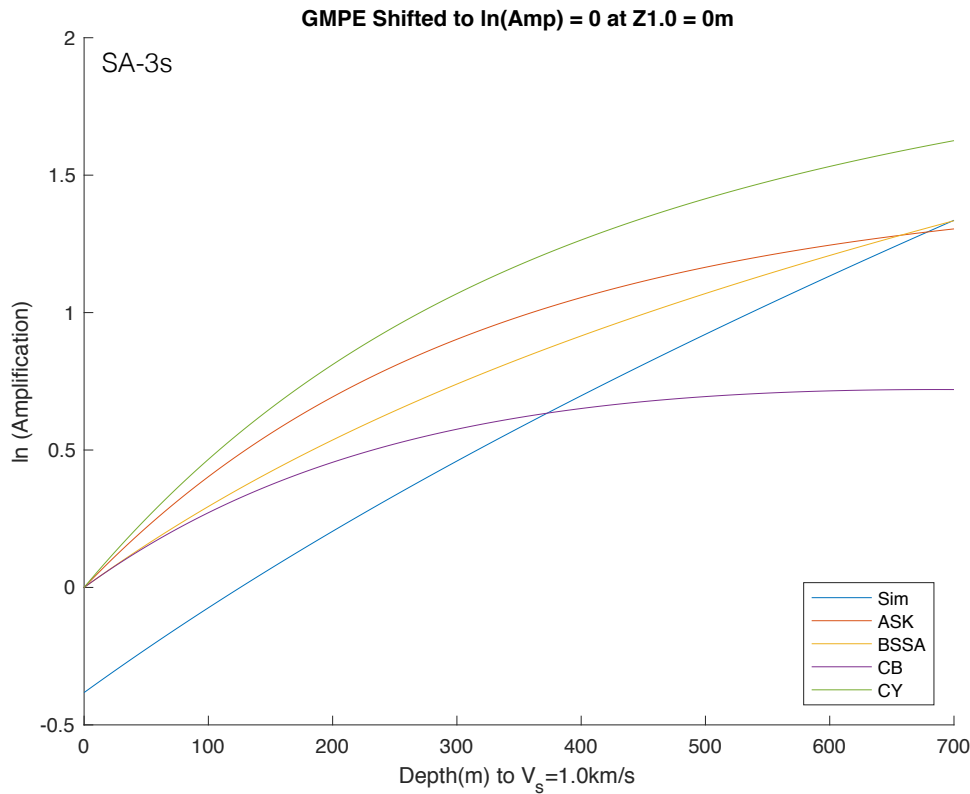


Figure 18. Same as Fig. 17, but for SA-3s.

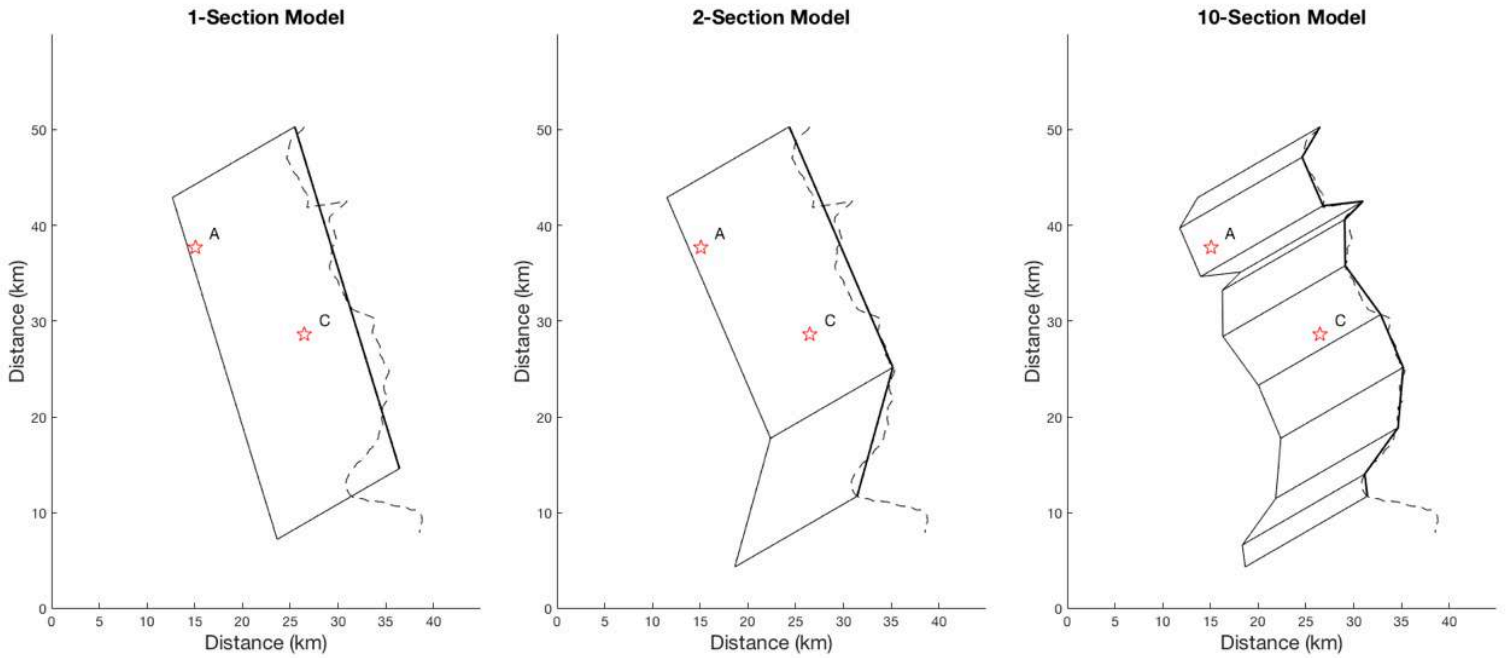


Figure 19. Surface projections of (left) 1-section, (middle) 2-section, and (right) 10-section WFSLC approximation models used in the calculation of directivity factors with the Bayless et al. (2013) model. The solid lines are the boundaries of the fault sections, with the upper boundaries shown in bold. Red stars depict the epicenters for Scenarios A and C. The dashed line shows the WFSLC trace from the simulations.

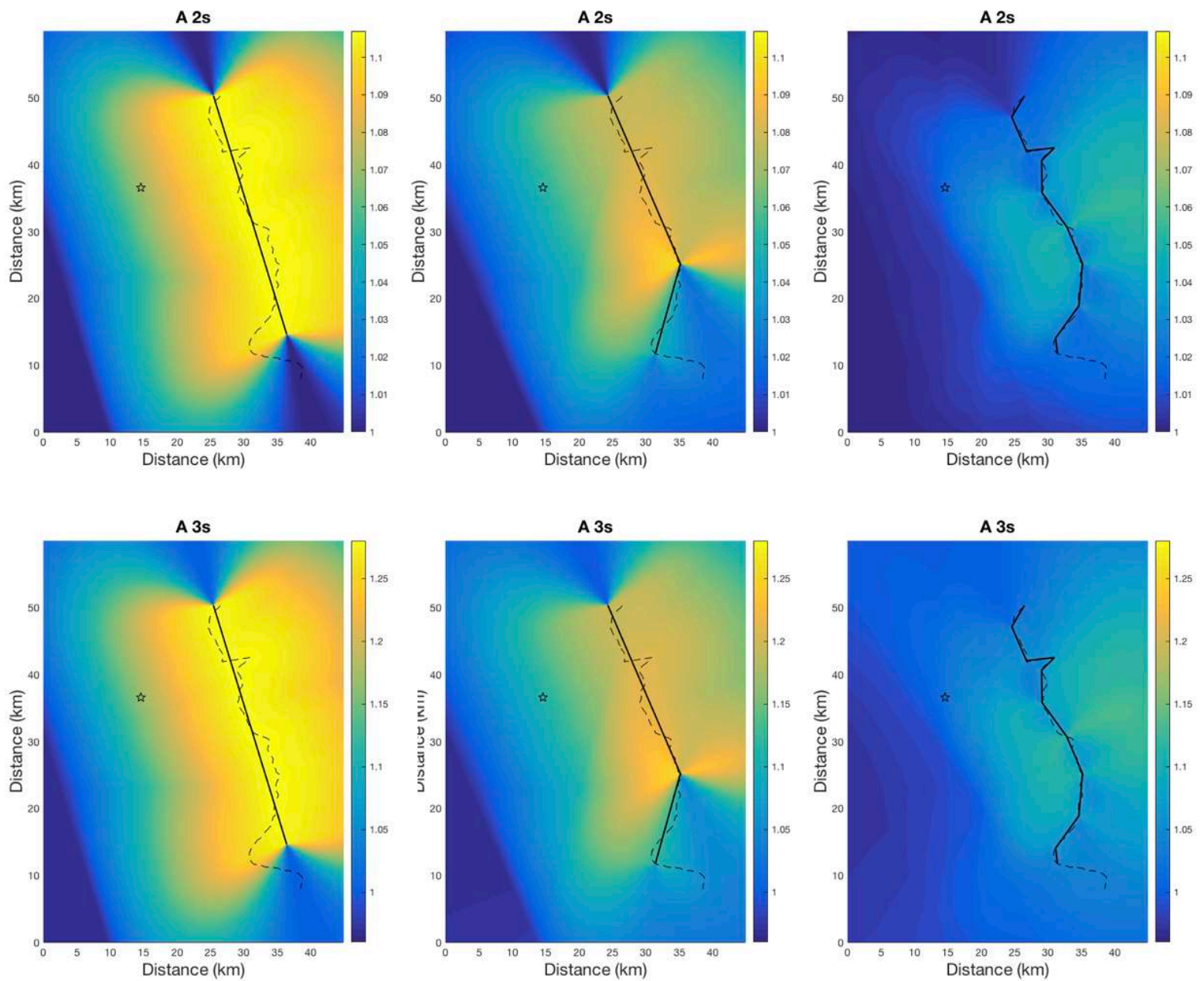


Figure 20. Maps of the directivity factors calculated from the 1-section (left), 2-section (middle), and 10-section (right) WFSLC approximation models for scenario A at 2s period (top) and 3s period (bottom). The solid lines are surface trace sections and the dashed lines are the actual WFSLC trace. The star depicts the epicenter.

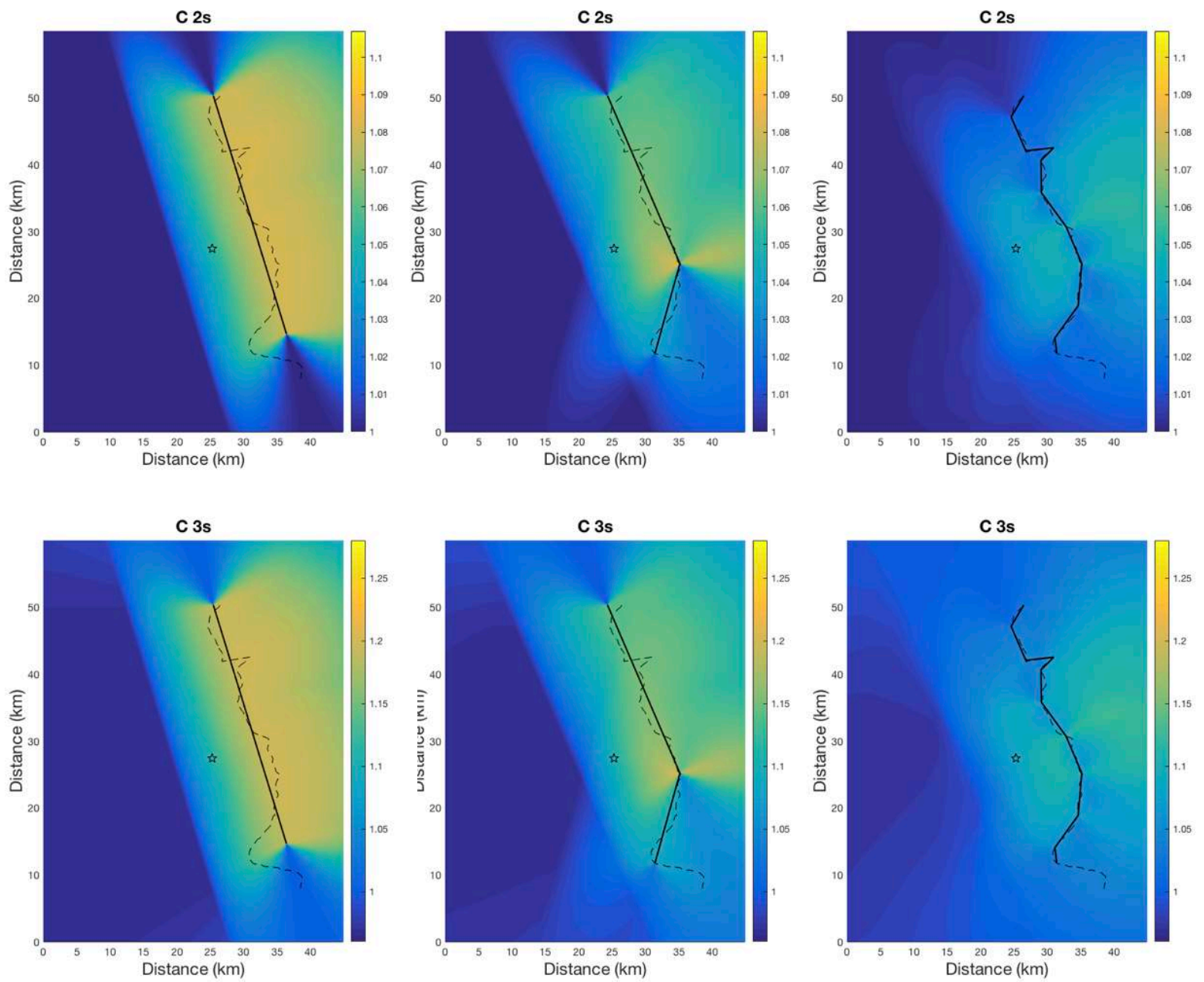


Figure 21. Same as Fig. 20, but for Scenario C.

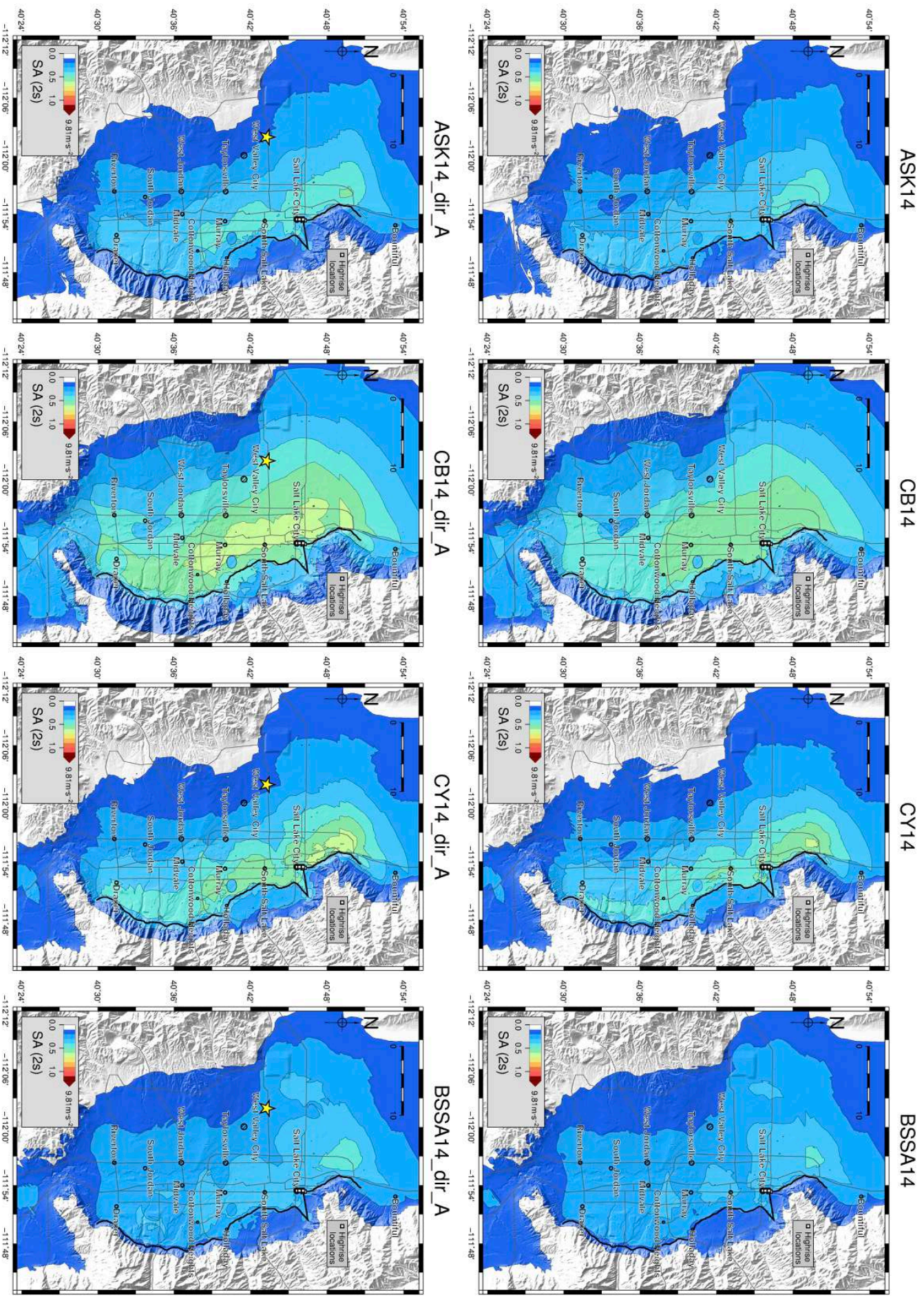


Figure 22. SA-2s for Scenario A. (top, from left to right) ASK14, CB14, CY14, and BSSA14.(bottom, from left to right) ASK14_dir, which is ASK14 modified with directivity factors from Bayless and Somerville (2013), CB14_dir, CY14_dir, and BSSA14_dir. All of the GMPE predictions are for the 3D model. The star depicts the epicenter, the bold line the fault surface trace.

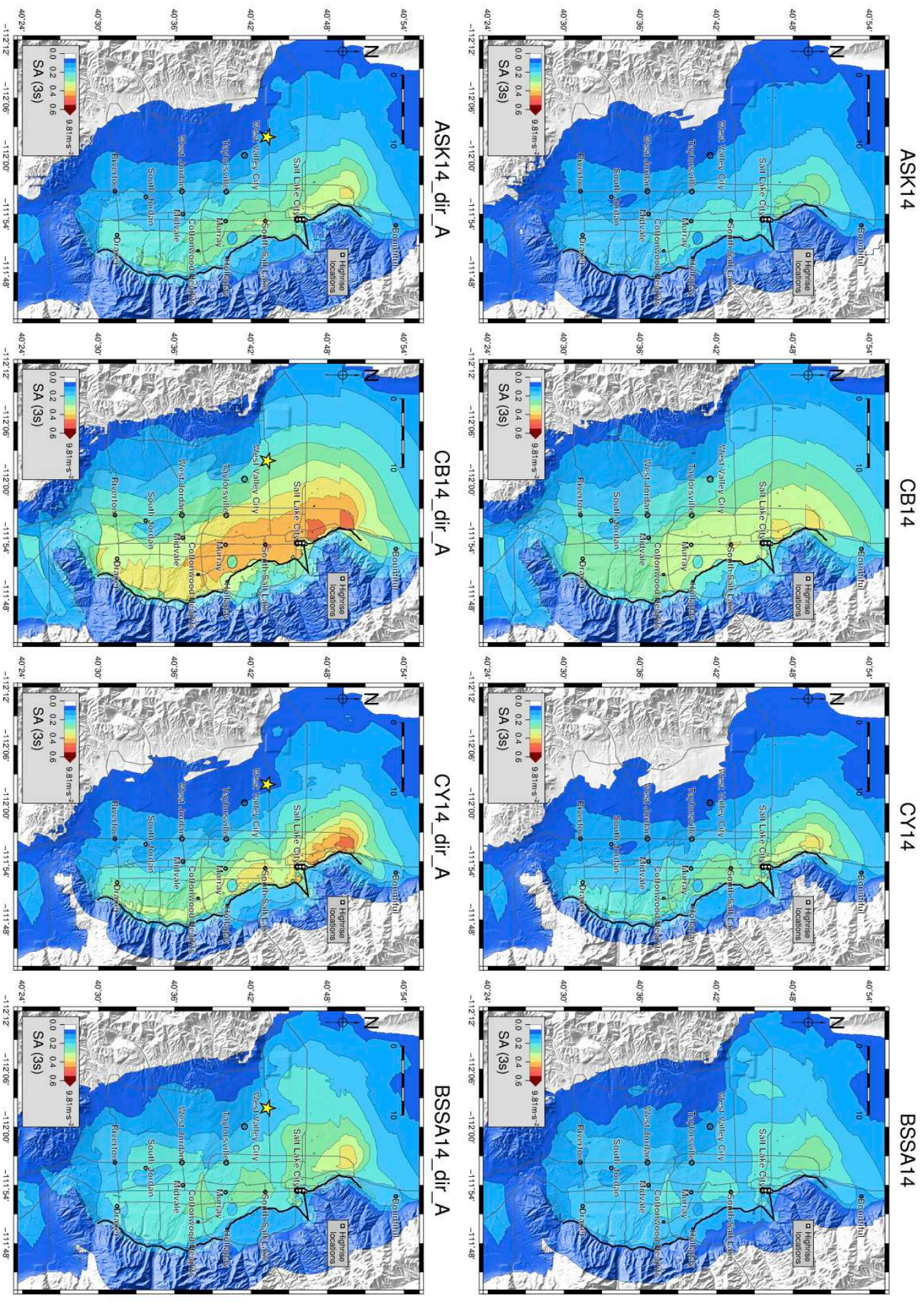


Figure 23. Same as Fig. 22, but for SA-3s.

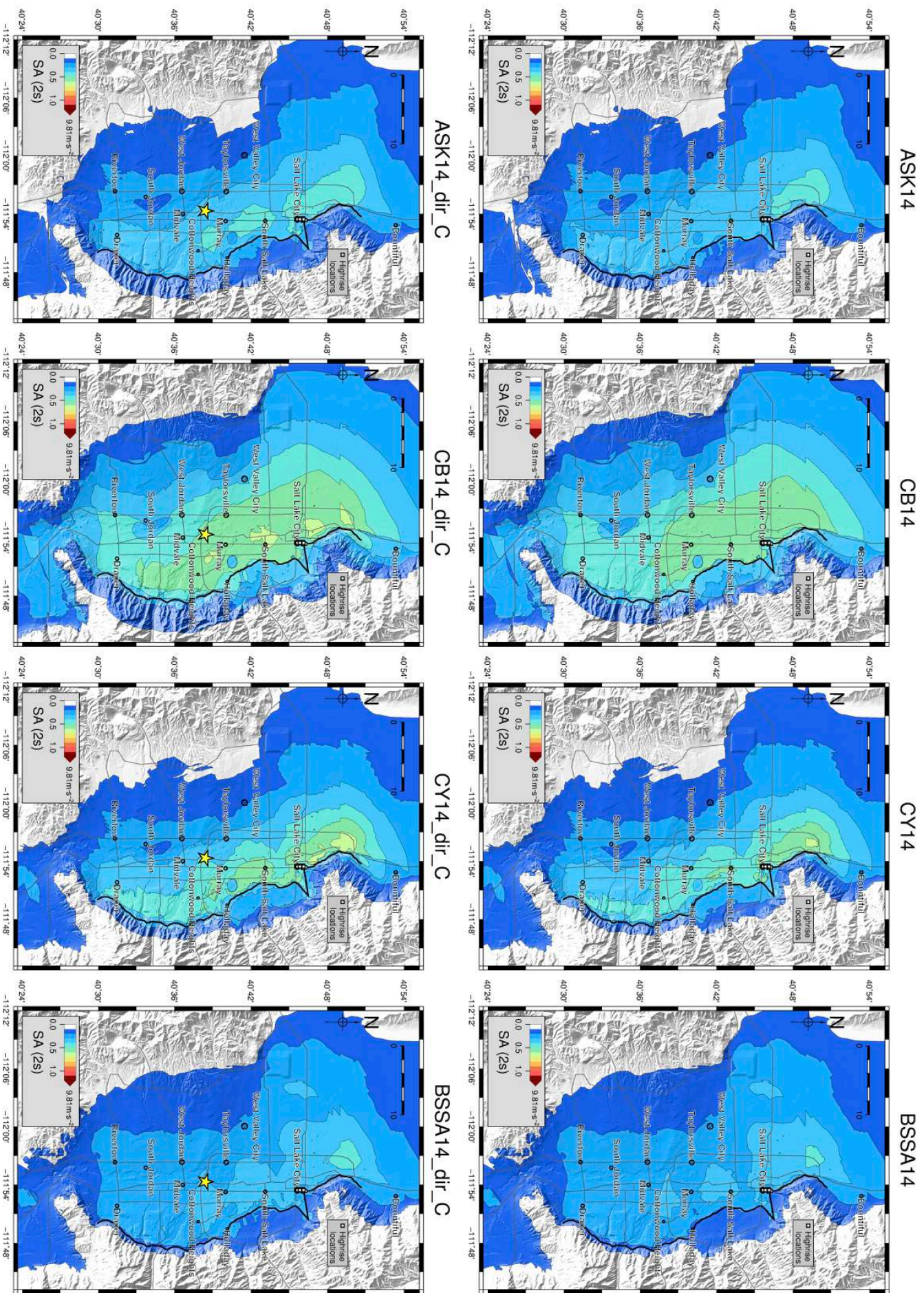


Figure 24. Same as Fig. 22, but for Scenario C.

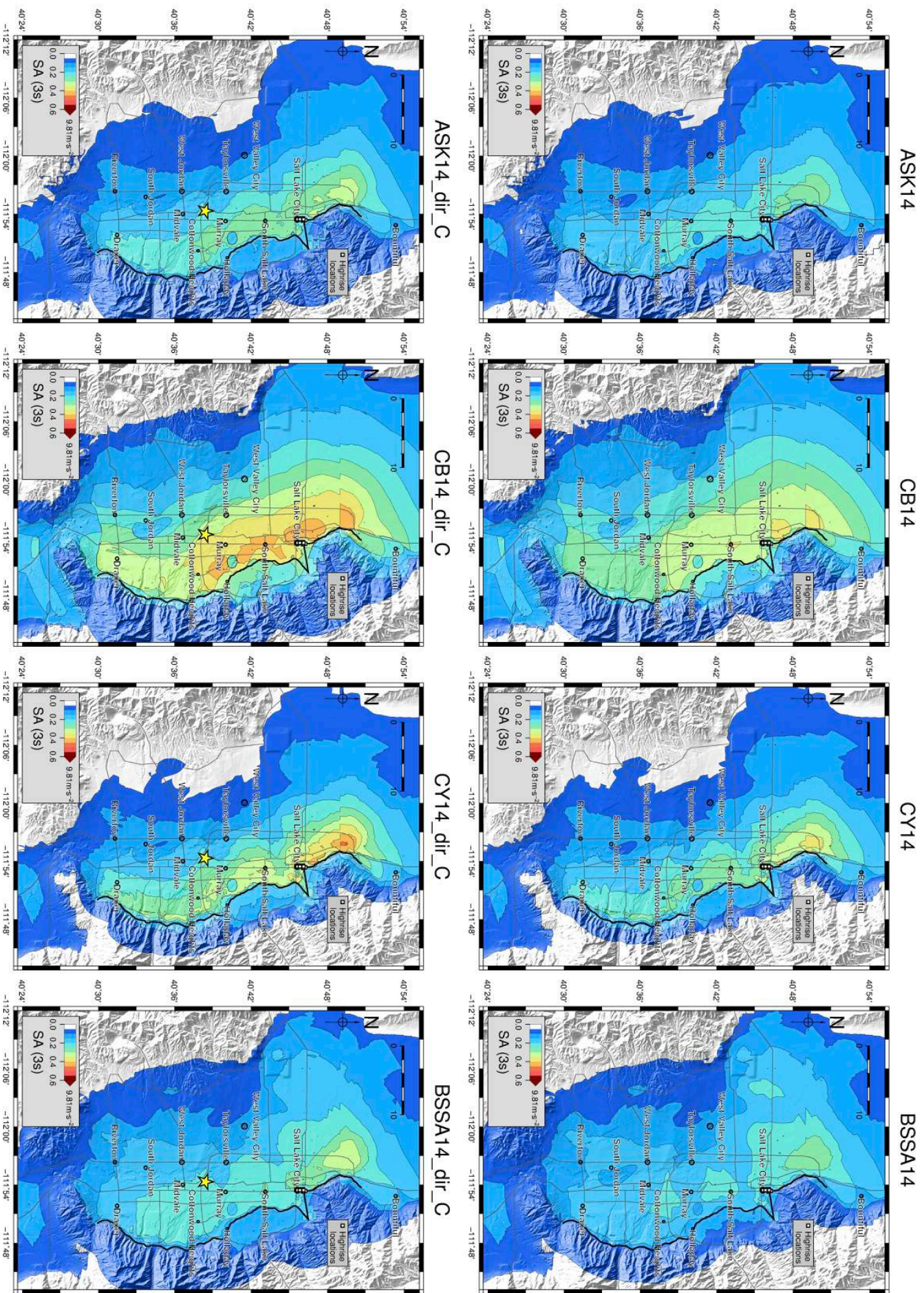
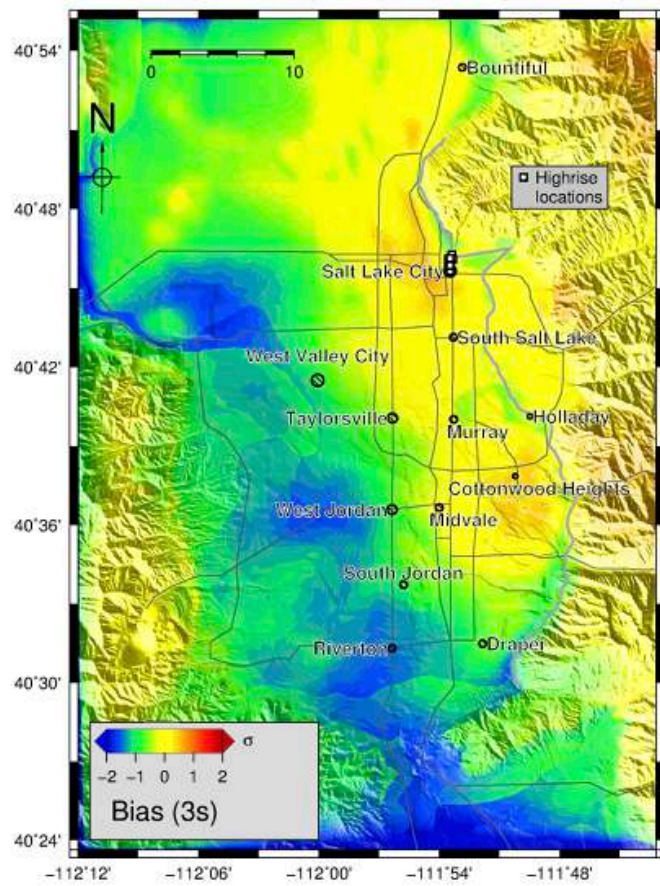


Figure 25. Same as Fig. 23, but for Scenario C.

BSSA14



CB14

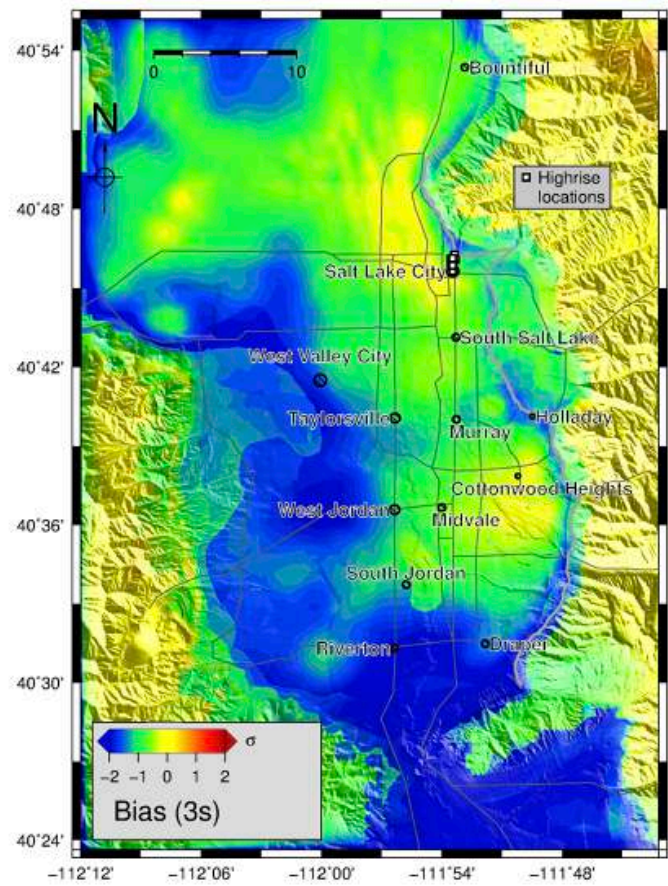
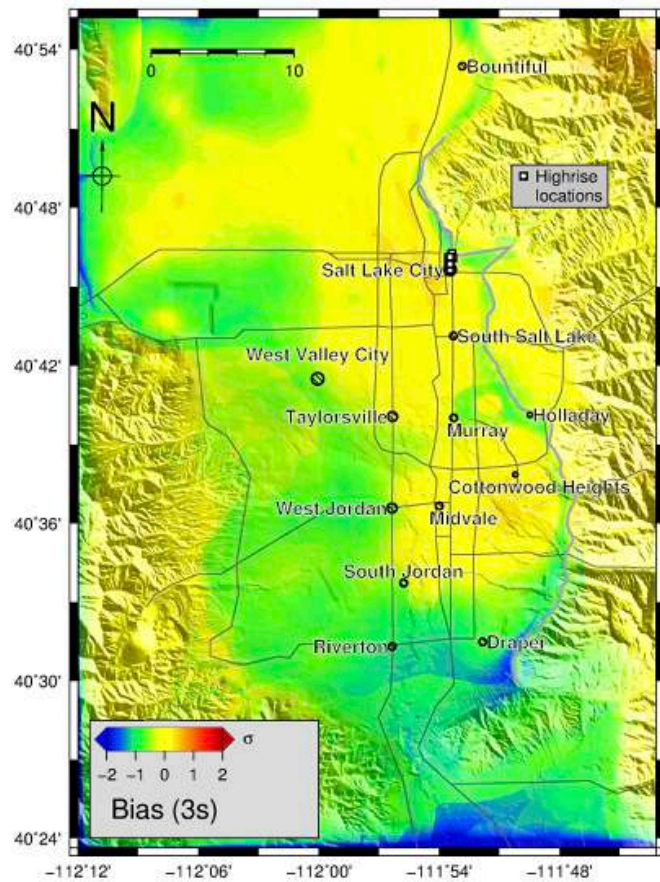


Figure 26. Bias between the ensemble of SA-3s(3D) and (left) BSSA14 and (right) CB14.

ASK14



CY14

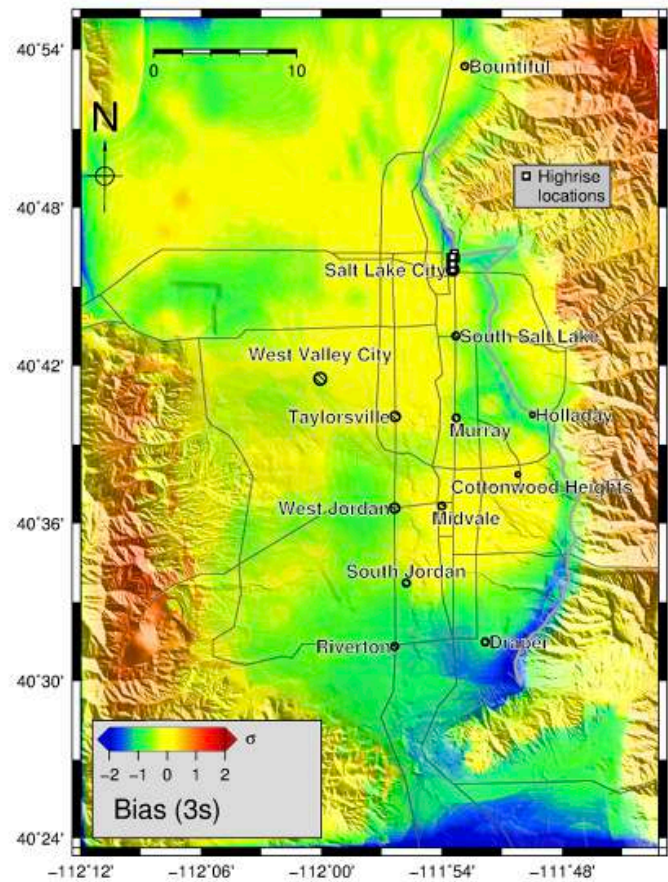
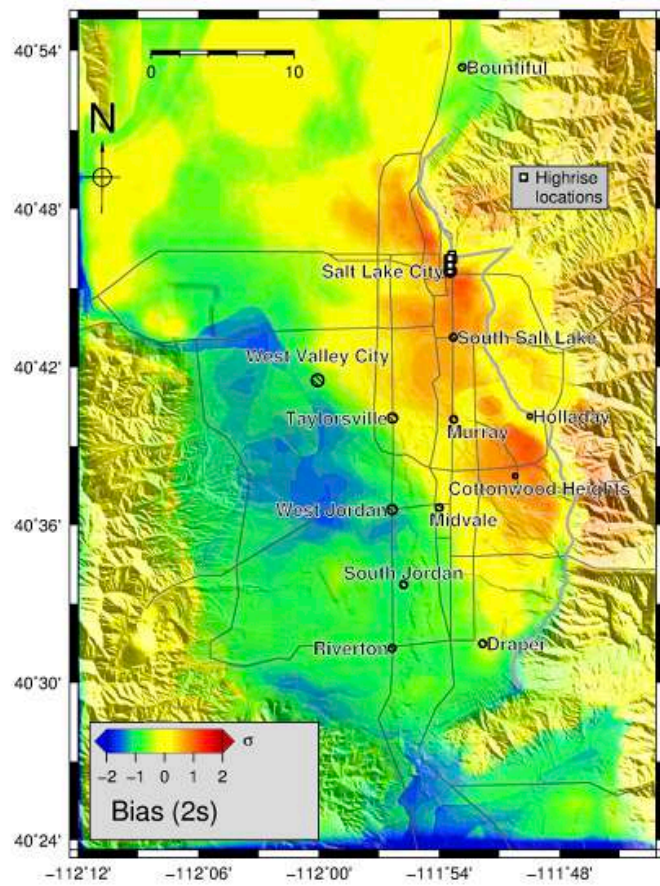


Figure 27. Bias between the ensemble of SA-3s(3D) and (left) ASK14 and (right) CY14.

BSSA14



CB14

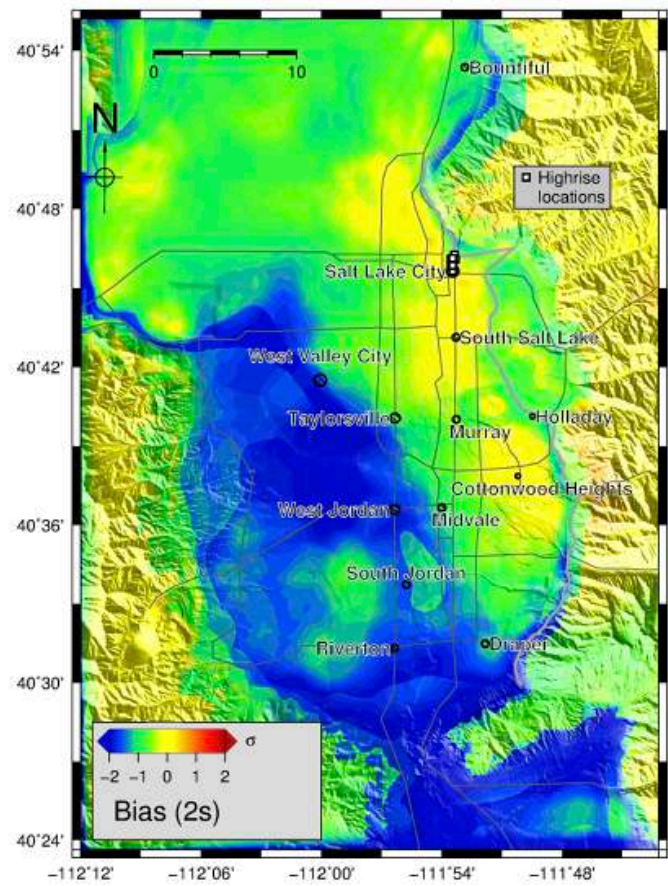
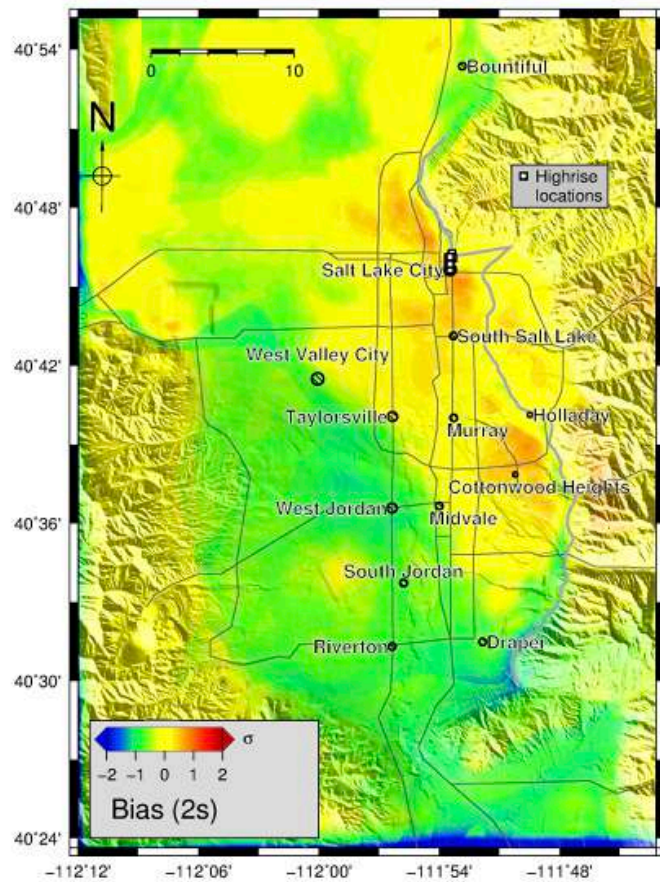


Figure 28. Bias between the ensemble of SA-2s(3D) and (left) BSSA14 and (right) CB14.

ASK14



CY14

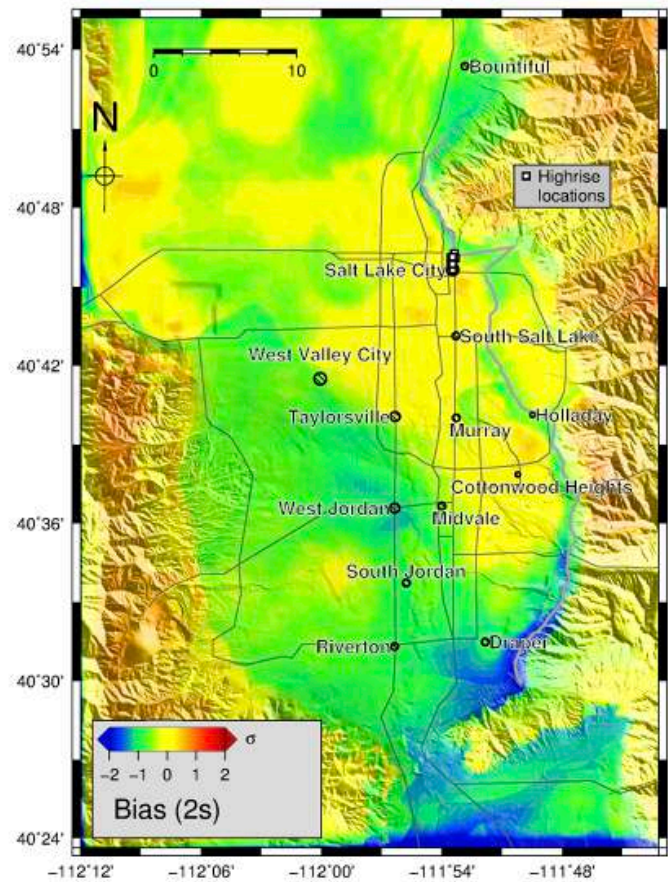


Figure 29. Bias between the ensemble of SA-2s(3D) and (left) ASK14 and (right) CY14.

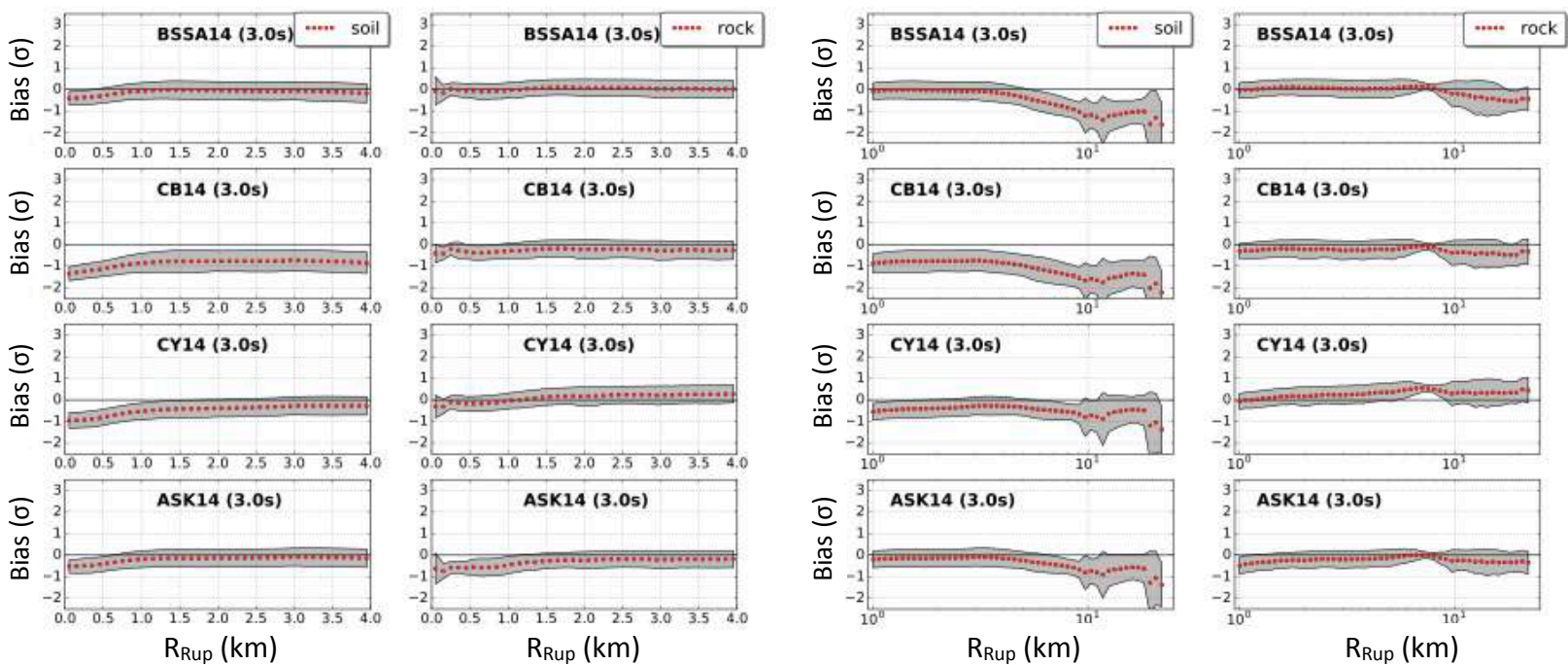


Figure 30. Bias between the 6-scenario ensemble of SA-3s(3D) and four leading NGA-West2 GMPEs for soil sites ($V_{s30} < 750$ m/s) and rock sites ($V_{s30} > 750$ m/s) as indicated. Note the difference in distance scales between the plots on the left and right sides. The shaded areas show the standard deviations of the residuals.

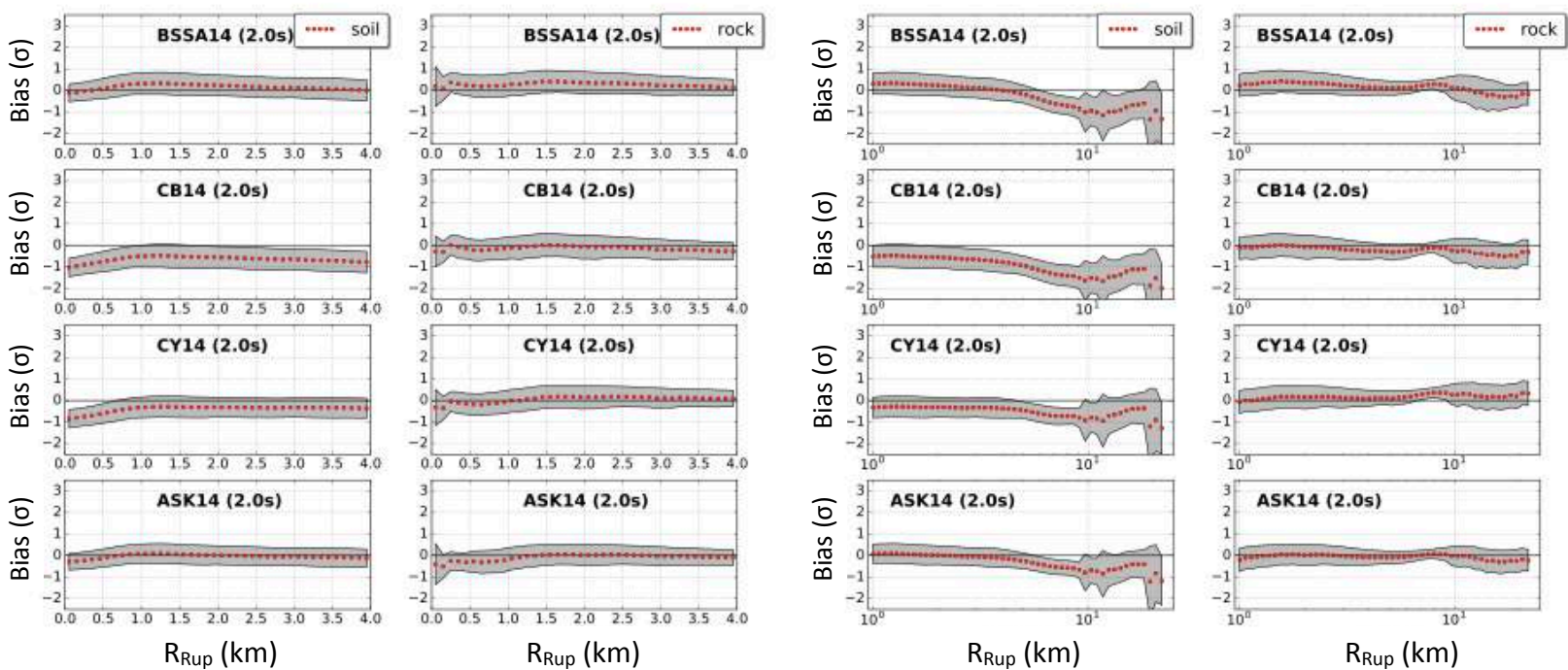
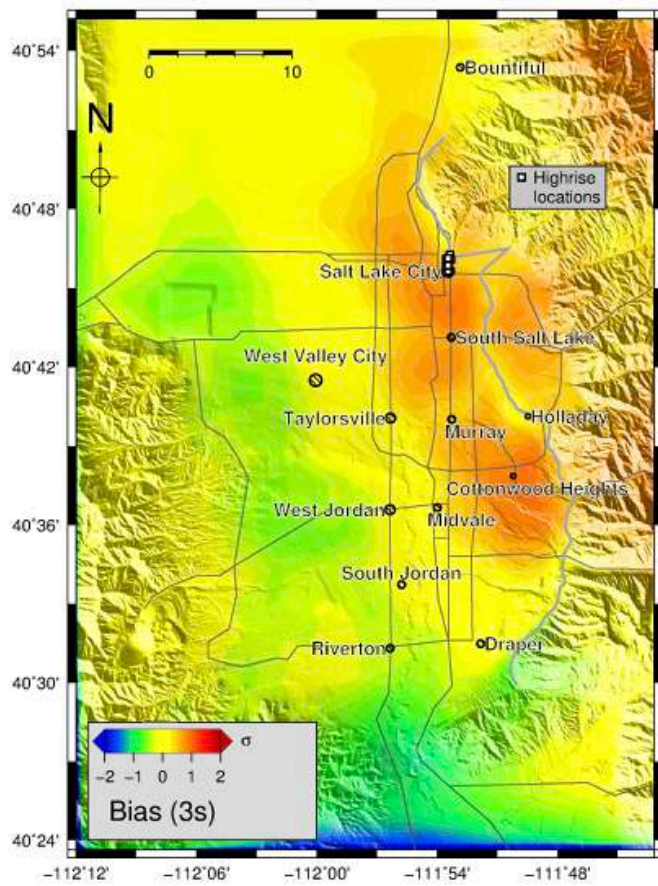


Figure 31. Same as Fig. 30, but for SA-2s.

BSSA14



CB14

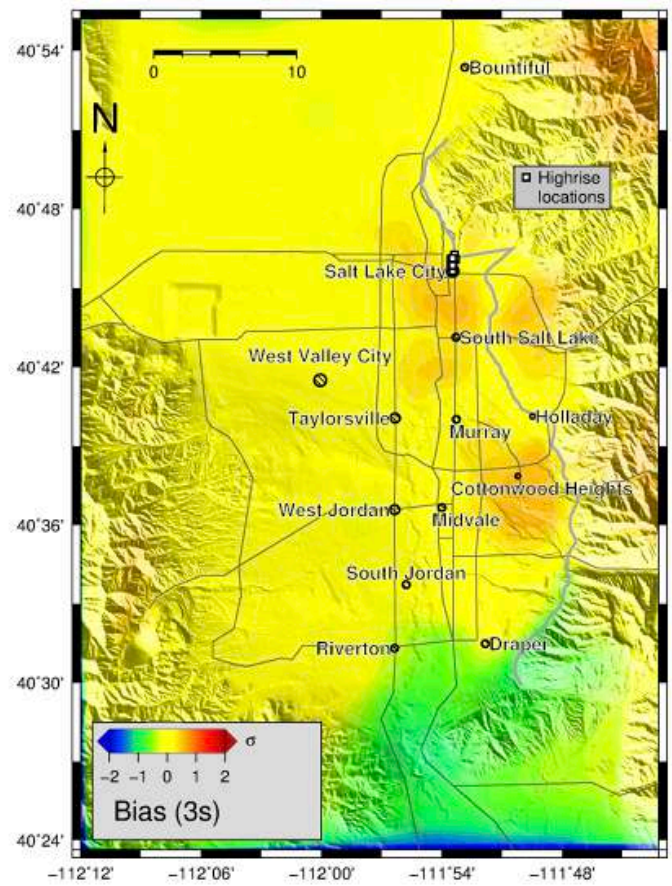
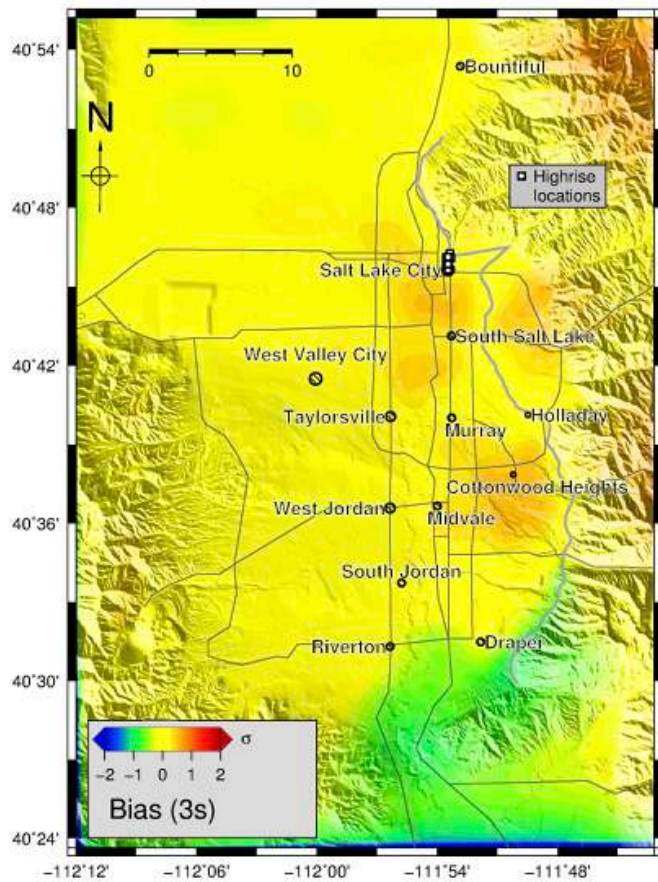


Figure 32. Bias between the ensemble of SA-3s(1D) and (left) BSSA14 and (right) CB14.

ASK14



CY14

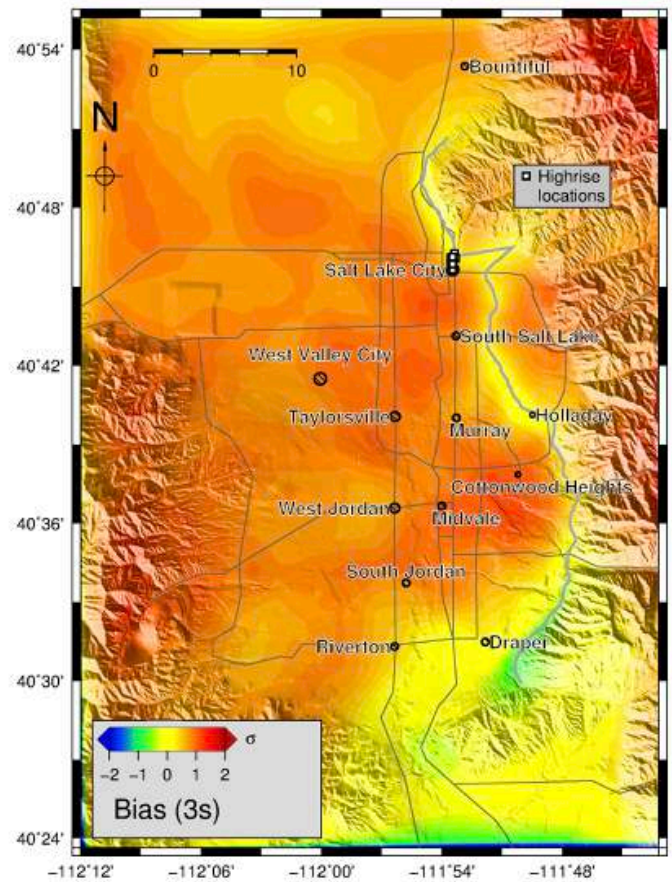
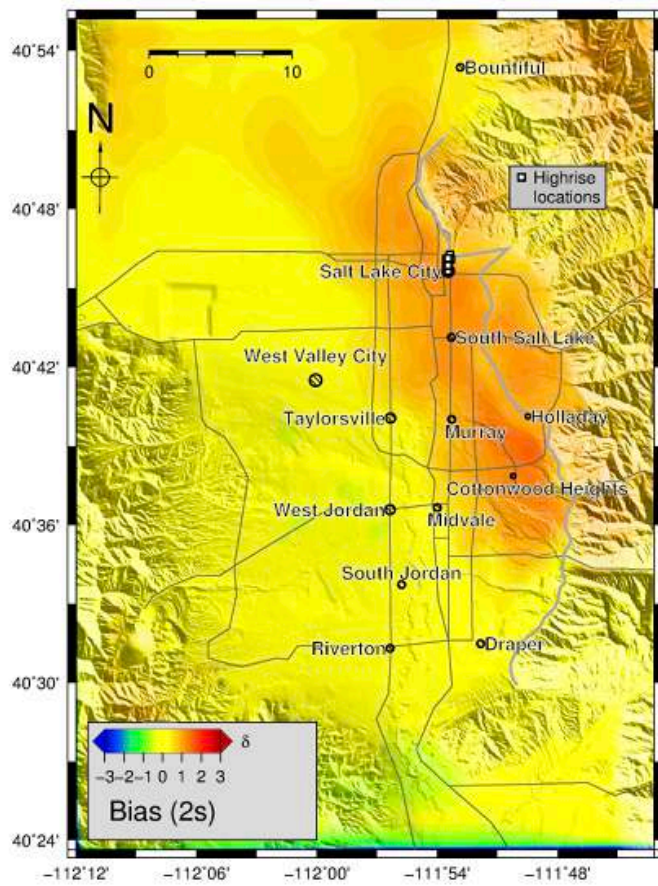


Figure 33. Bias between the ensemble of SA-3s(1D) and (left) ASK14 and (right) CY14.

BSSA14



CB14

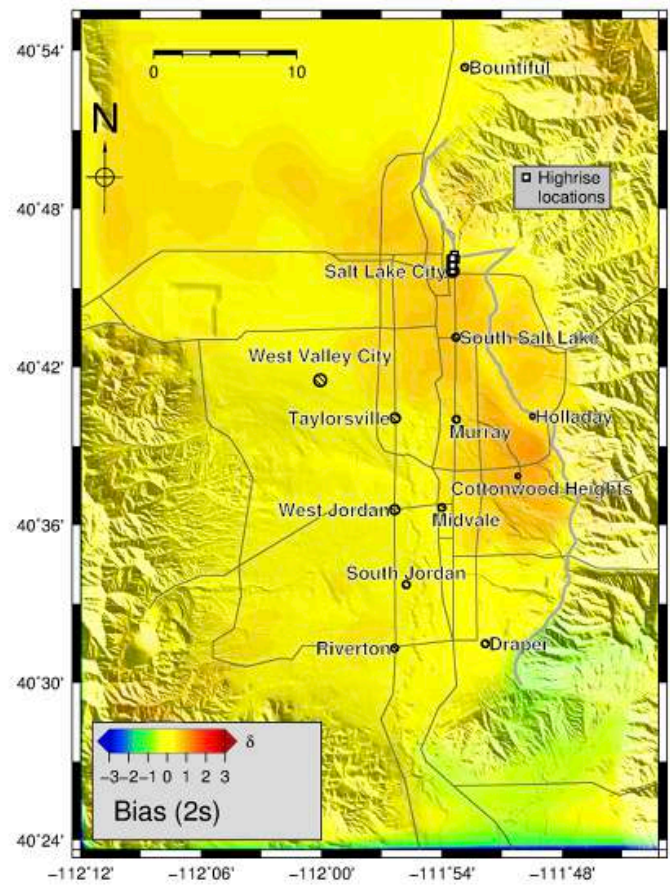
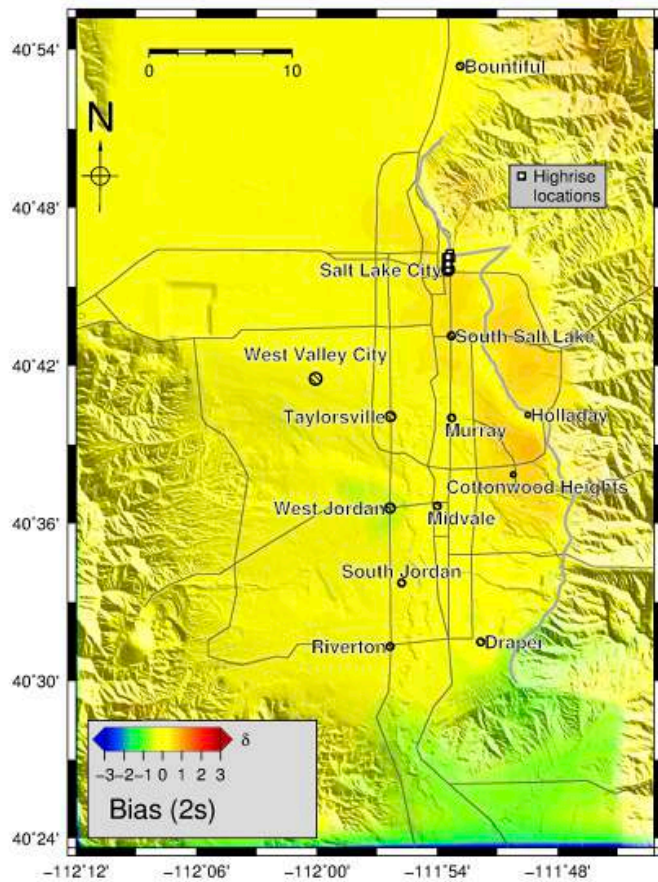


Figure 34. Bias between the ensemble of SA-2s(1D) and (left) BSSA14 and (right) CB14.

ASK14



CY14

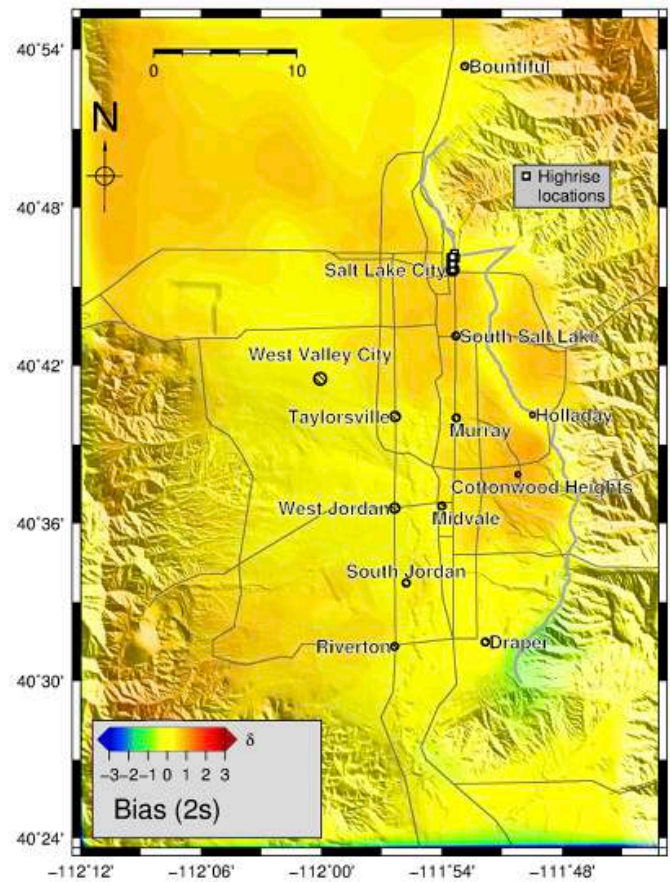


Figure 35. Bias between the ensemble of SA-2s(1D) and (left) ASK14 and (right) CY14.

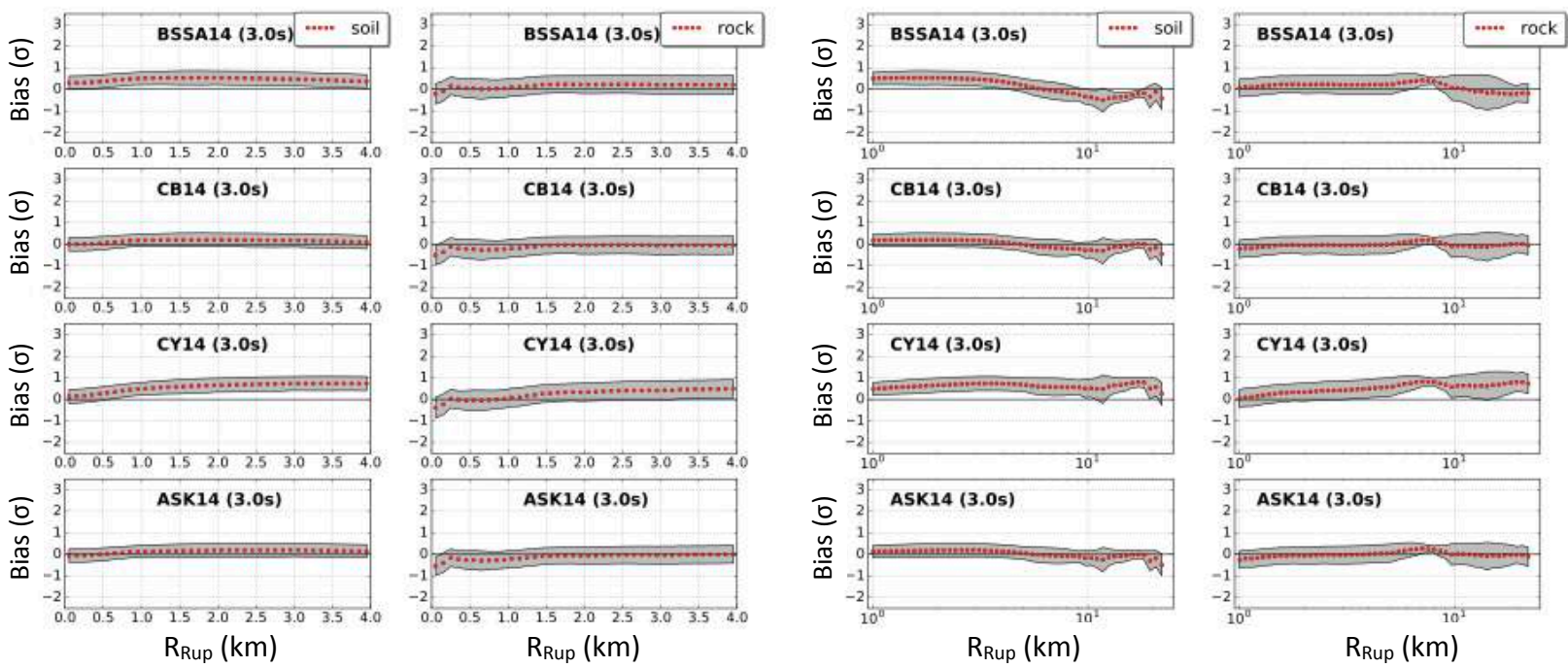


Figure 36. Bias between the 6-scenario ensemble of SA-3s(1D) and four leading NGA-West2 GMPEs for soil sites ($V_{s30} < 750$ m/s) and rock sites ($V_{s30} > 750$ m/s) as indicated. Note the difference in distance scales between the plots on the left and right sides. The shaded areas show the standard deviations of the residuals.

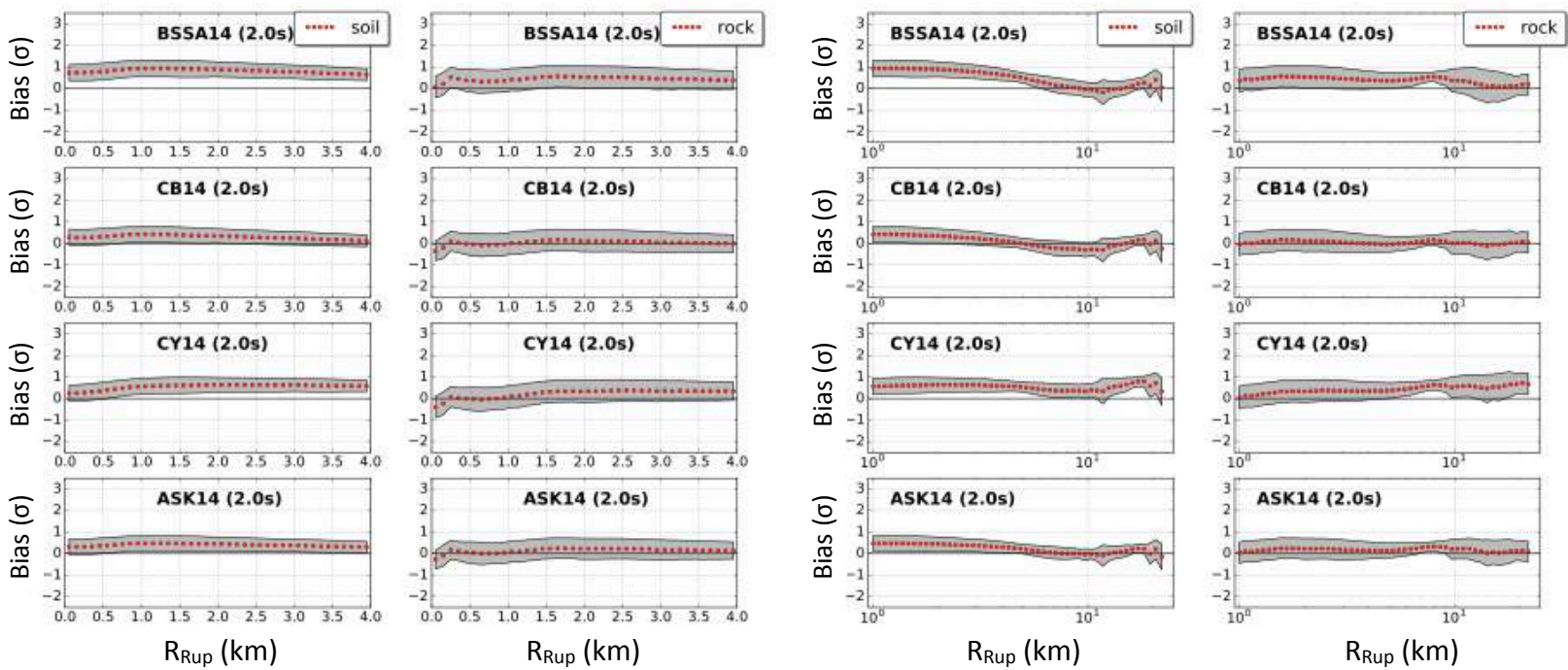


Figure 37. Same as Fig. 36, but for SA-2s.

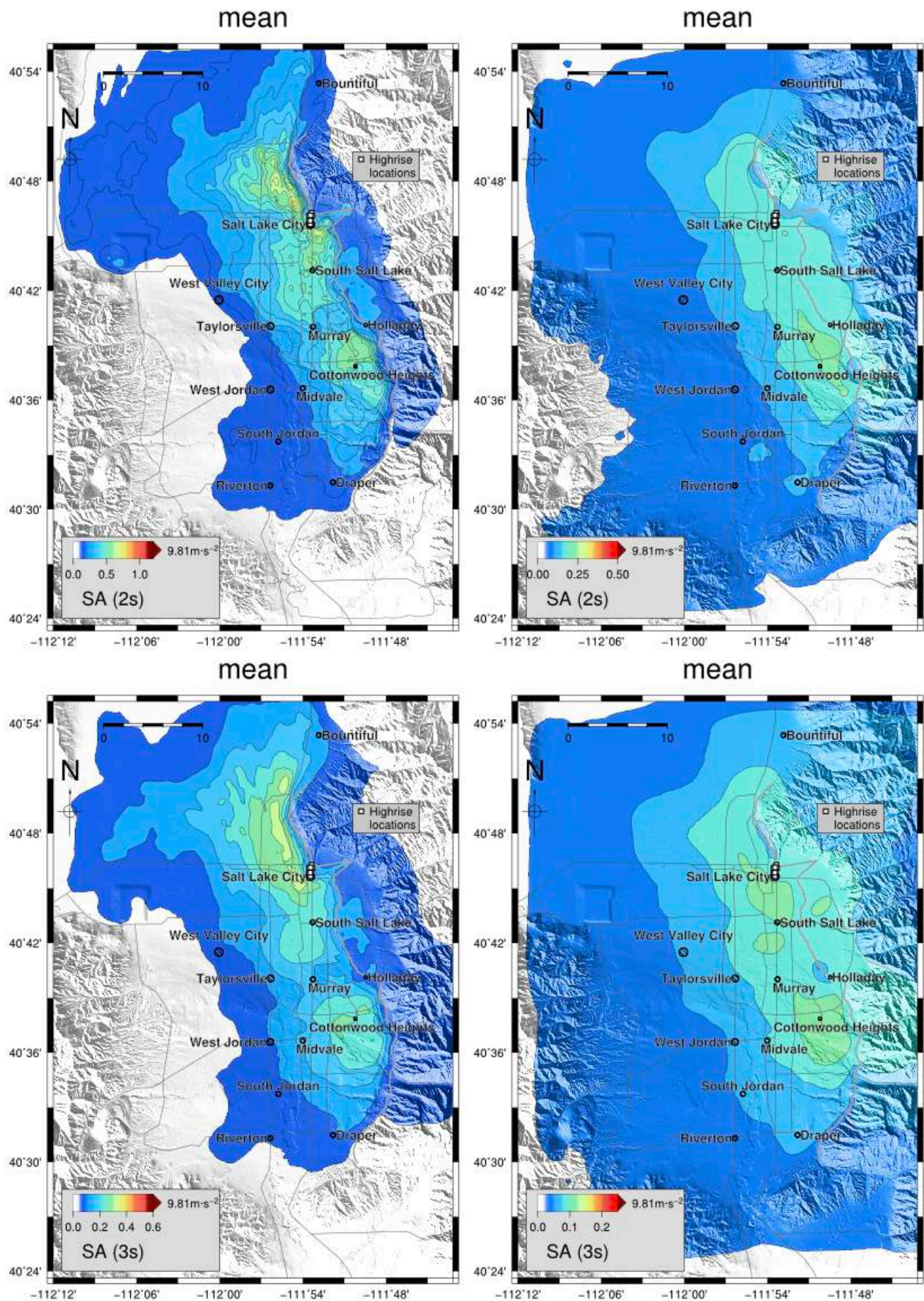


Figure 38. Maps of the geometric mean (top) SA-2s and (bottom) SA-3s values for the six scenarios in the (left) 3D WFCVM model and (right) 1D rock model. The bold grey line depicts the fault surface trace.

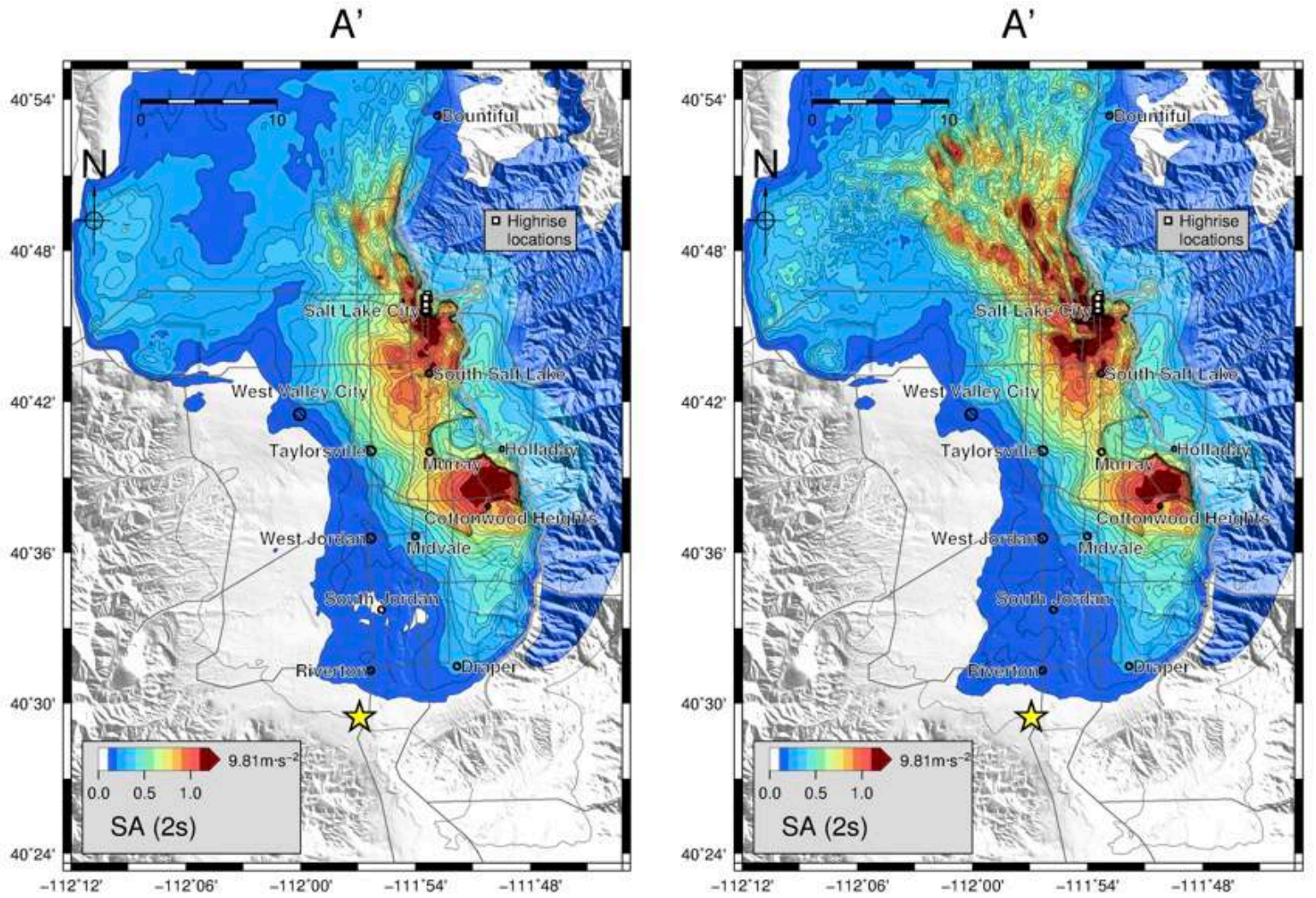


Figure 39. Comparison of SA-2s distributions for scenario A', calculated using (left) the Brocher (2006) Q relations as in Roten et al. (2011) and right, $Q_s=0.1V_s$ (V_s in km/s) and $Q_p=2Q_s$ (Withers et al., 2015).

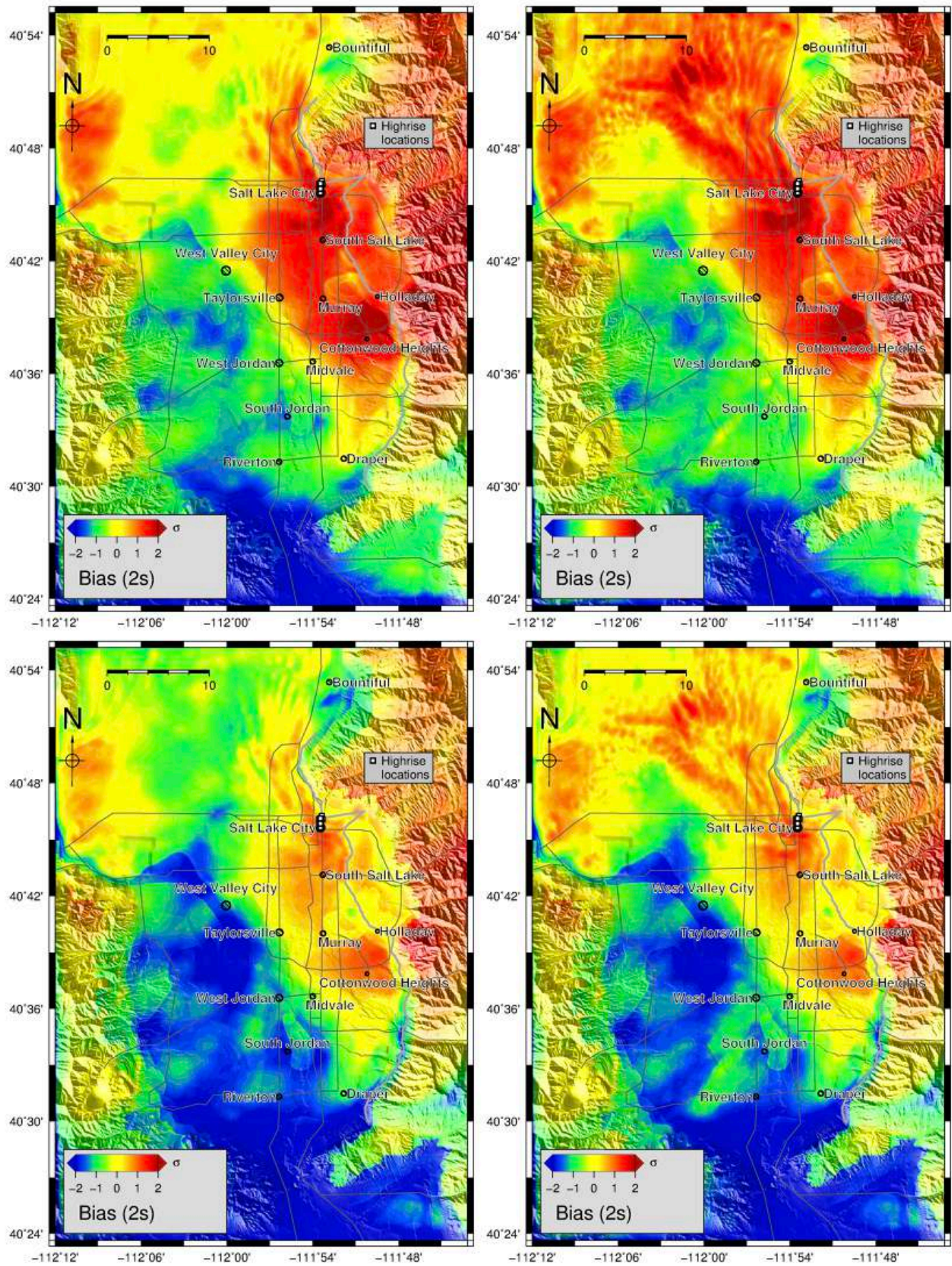


Figure 40. Comparison of bias between SA-2s distributions for scenario A' relative to (top) BSSA14 and (bottom) CB14, calculated using (left) the Brocher (2006) Q relations as in Roten et al. (2011) and right, $Q_s = 0.1V_s$ (V_s in km/s) and $Q_p = 2Q_s$ (Withers et al., 2015).

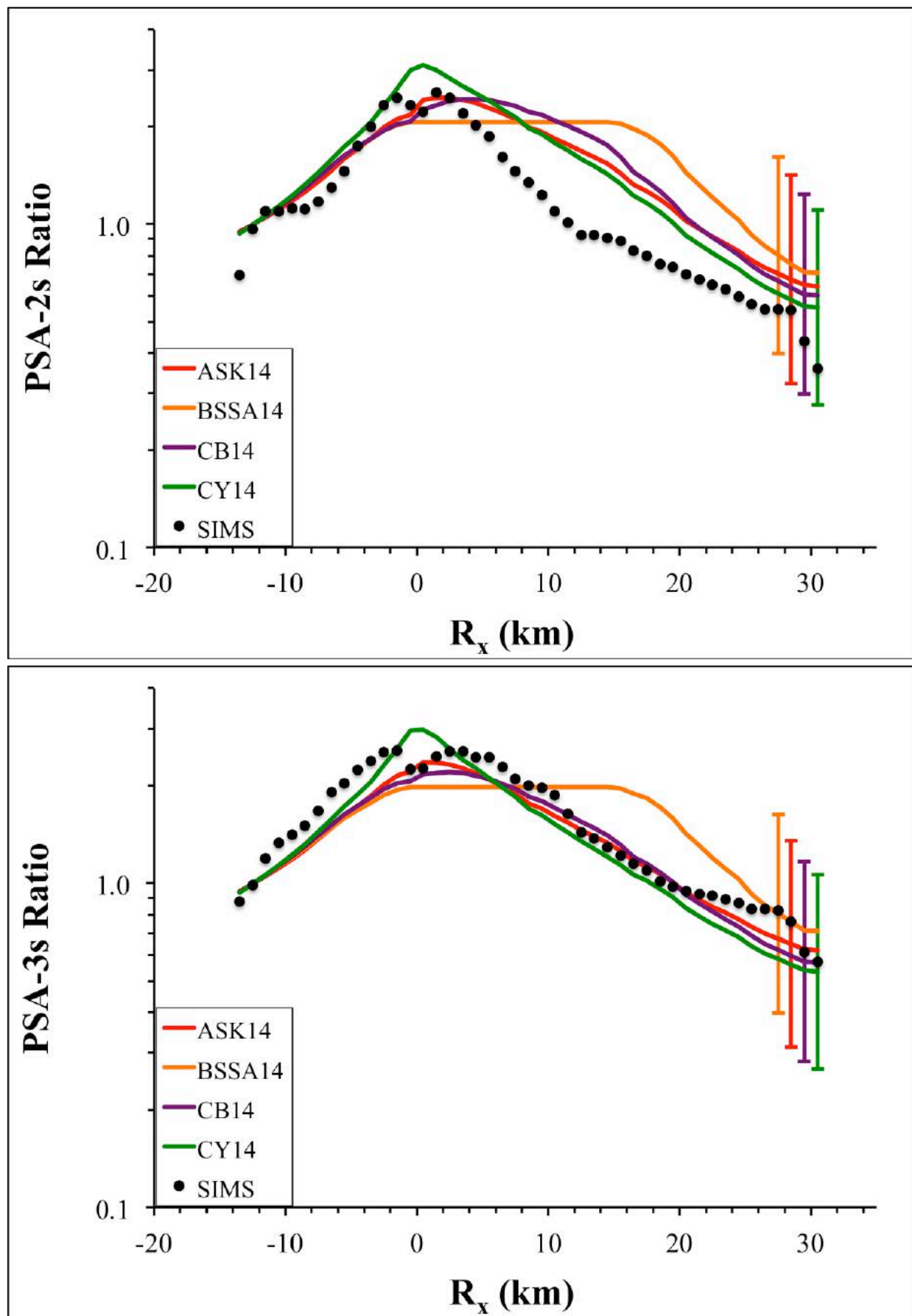


Figure 41. Comparison of geometric mean (top) SA-2s and (bottom) SA-3s from the six scenarios (black dots) with GMPE predictions (colored lines with 1 standard deviation error bars) for sites within a 4-km-wide zone trending ENE-WSW across the rupture center. R_x is horizontal distance from the top of the rupture, measured perpendicular to its strike. All SAs are normalized to 1.0 at a site where $R_x = -12.2$ km. The results plotted are geometric means for 1-km R_x bins.